NASA/TM–2009–000000

Honeycomb vs. Foam: Evaluating a Potential Upgrade to ISS Module Shielding for Micrometeoroids and Orbital Debris

Shannon Ryan
USRA Lunar and Planetary Institute
Johnson Space Center, Houston, Texas

Troy Hedman
GeoControl Systems, Inc. (ESCG)
Johnson Space Center, Houston, Texas

Eric L. Christiansen
Johnson Space Center, Houston, Texas

September 2009

NASA STI Program ... in Profile

Since its founding, NASA has been dedicated to the advancement of aeronautics and space science. The NASA scientific and technical information (STI) program plays a key part in helping NASA maintain this important role.

The NASA STI program operates under the auspices of the Agency Chief Information Officer. It collects, organizes, provides for archiving, and disseminates NASA's STI. The NASA STI program provides access to the NASA Aeronautics and Space Database and its public interface, the NASA Technical Report Server, thus providing one of the largest collections of aeronautical and space science STI in the world. Results are published in both non-NASA channels and by NASA in the NASA STI Report Series, which includes the following report types:

- TECHNICAL PUBLICATION. Reports of completed research or a major significant phase of research that present the results of NASA Programs and include extensive data or theoretical analysis. Includes compilations of significant scientific and technical data and information deemed to be of continuing reference value. NASA counterpart of peer-reviewed formal professional papers but has less stringent limitations on manuscript length and extent of graphic presentations.

- TECHNICAL MEMORANDUM. Scientific and technical findings that are preliminary or of specialized interest, e.g., quick release reports, working papers, and bibliographies that contain minimal annotation. Does not contain extensive analysis.

- CONTRACTOR REPORT. Scientific and technical findings by NASA-sponsored contractors and grantees.

- CONFERENCE PUBLICATION. Collected papers from scientific and technical conferences, symposia, seminars, or other meetings sponsored or co-sponsored by NASA.

- SPECIAL PUBLICATION. Scientific, technical, or historical information from NASA programs, projects, and missions, often concerned with subjects having substantial public interest.

- TECHNICAL TRANSLATION. English-language translations of foreign scientific and technical material pertinent to NASA's mission.

Specialized services also include creating custom thesauri, building customized databases, and organizing and publishing research results.

For more information about the NASA STI program, see the following:

- Access the NASA STI program home page at *http://www.sti.nasa.gov*

- E-mail your question via the Internet to help@sti.nasa.gov

- Fax your question to the NASA STI Help Desk at 443-757-5803

- Phone the NASA STI Help Desk at 443-757-5802

- Write to:
  NASA STI Help Desk
  NASA Center for AeroSpace Information
  7115 Standard Drive
  Hanover, MD 21076-1320

NASA/TM–2009–000000

Honeycomb vs. Foam: Evaluating a Potential Upgrade to ISS Module Shielding for Micrometeoroids and Orbital Debris

Shannon Ryan
USRA Lunar and Planetary Institute
Johnson Space Center, Houston, Texas

Troy Hedman
GeoControl Systems, Inc. (ESCG)
Johnson Space Center, Houston, Texas

Eric L. Christiansen
Johnson Space Center, Houston, Texas

National Aeronautics and
Space Administration

Johnson Space Center
Houston, TX 77058

September 2009

Acknowledgements

All testing was performed at the NASA Johnson Space Center White Sands Test Facility in Las Cruces, N.M.

Available from:

NASA Center for AeroSpace Information
7115 Standard Drive
Hanover, MD 21076-1320
Phone: 301-621-0390 or
Fax: 301-621-0134

National Technical Information Service
5285 Port Royal Road
Springfield, VA 22161
703-605-6000

This report is also available in electronic form at http://ston.jsc.nasa.gov/collections/TRS/

Contents

Introduction 1
Background 1
  Hypervelocity Impact Performance of Honeycomb Sandwich Panels 1
  Hypervelocity Impact Performance of Metallic Open-Cell Foams................................ 2
  Definition and Properties of Aluminum Open-Cell Foam 6
Target Description 7
  Double Layer Honeycomb (DL-H) 7
  Double Layer Foam (DL-F)... 7
Test Results 9
  Evaluation of Shield Modification 9
  The Effect of Impact Angle on Shield Performance 17
  A Ballistic Limit for the Double-Layer Foam Shield Configuration............................. 19
  Additional Test Data 25
  Comparison of DL-H and DL-F Ballistic Limit Predictions.. 26
Discussion...28
Conclusions 30
References 31

Figures

Figure 1: Rear wall sizing for a dual-wall shield with (Sennett & Lathrop, Taylor) and without (Cour-Palais NO) a honeycomb core. 2
Figure 2: Internal honeycomb damage following impact of a 3.0 mm diameter 99.9% Al-sphere at 60° with a velocity of 6.29 km/s. 3
Figure 3: Damage to a sandwich panel with 1.37mm thick CFRP facesheets and a 25mm thick 3/16-5056-.001 honeycomb core impacted at 60° by a 3.0mm Al99.9% projectile at 6.29 km/s. Left: Front facesheet damage; Right: Rear facesheet damage showing two perforation holes related (1) to the debris ejected at normal incidence to the front facesheet and (2) along the projectile velocity vector. 3
Figure 4: Alternate Columbus MMOD shield configuration incorporating metallic open-cell foam (from [7]). 4
Figure 5: Comparison of damages in a open cell foam core (left) and honeycomb core (right) sandwich panel structures impacted by a 3.6 mm Al-sphere at 6.49±0.27 km/s (0°). Upper: front facesheet damage; Middle: core damage (sectioned); Bottom: rear facesheet damage. (from [8]). 5
Figure 6: Definition of open cell foam pore and cell size (© ERG Aerospace). 6
Figure 7: Ligament cross section shape variation with relative density (© ERG Aerospace). 6
Figure 8: Schematic of the double layer honeycomb target configuration. 7
Figure 9: Characterization of the 10 PPI foam structure. Cell size (1) = 3.95 mm, pore size (3) = 2.33 mm, ligament width (2) = 382 μm. 8
Figure 10: Schematic of the double layer foam target configuration. 8
Figure 11: Comparison of impact damages in the DL-H (left) and DL-F (right) targets impacted by a 0.833 cm diameter Al 2017-T4 sphere at ~6.9 km/s and 0°. From top to bottom: 1st mesh layer (front view), 2nd mesh layer (front view), 1st sandwich panel (front view). 11
Figure 12: Comparison of impact damages in the DL-H (left) and DL-F (right) targets impacted by a 0.873 cm diameter Al 2017-T4 sphere at ~6.6 km/s and 45°. From top to bottom: 1st mesh layer (front view), 2nd mesh layer (front view), 1st sandwich panel (front view). 14
Figure 13: Comparison of impact damages in the DL-H target rear wall impacted by 0.754 cm diameter Al 2017-T4 spheres at ~6.9 km/s with normal (left) and oblique (45°, right). 17
Figure 14: Comparison of impact damages in the DL-F target rear wall impacted by 1.005 cm diameter Al 2017-T4 spheres at ~6.9 km/s with oblique incidence. Left: 30°, right: 60°. 18
Figure 15: Melted aluminum deposits and solid fragment damage of the DL-F rear wall impacted by a 0.717 cm diameter projectile at 3.29 km/s with normal incidence (HITF08595). 18
Figure 16: Demonstrating the effect of the foam microstructure on projectile fragmentation and melt. Rear wall damage for the DL-H (upper) and DL-F (lower) shields impacted by 0.833 cm diameter projectiles at ~6.9 km/s and 0°. 20
Figure 17: Ballistic limit curve (original and modified) of the DL-H configuration for normal impact. 22
Figure 18: Ballistic limit curves of the double-layer foam shielding configuration at 0°. 23
Figure 19: Ballistic limit curves of the double-layer foam shielding configuration at 45°. 24
Figure 20: Ballistic limit curves of the double-layer foam shielding configuration at 60°. 24
Figure 21: Ballistic limit curve of the DL-H shield with 0.009" and 0.016" diameter wire mesh layers. 25
Figure 22: Ballistic limit curve of the DL-F shield with 0.009" and 0.016" diameter wire mesh layers. 26
Figure 23: Comparison between the DL-H and DL-F ballistic limit curves at 0°. 27
Figure 24: Comparison between the DL-H and DL-F ballistic limit curves at 45°. 27
Figure 25: Comparison between the DL-H and DL-F ballistic limit curves at 60°. 28
Figure 26: Solid fragment craters on the DL-F rear wall at high impact velocities (0.877 cm diameter Al2017-T4 sphere at normal incidence with 6.76 km/s). 29

Tables

Table 1: Description of double layer honeycomb target components. 7
Table 2: Description of double layer honeycomb target components. 8
Table 3: Hypervelocity impact test results. 9
Table 4: Constants of the FGB ballistic limit equation for the enhanced zone 11 shield. 21
Table 5: Modified constants of the FGB ballistic limit equation for the enhanced zone 11 shield. 22
Table 6: Additional hypervelocity impact test results. 25

Glossary of Terms and Abbreviations

Al	aluminum
BUMPER	software application used for spacecraft MMOD risk assessments
Bumper	outermost shield layer used to break up MMOD particles
BLE	ballistic limit equation
CFRP	carbon fiber reinforced plastic
DL-F	double layer foam
DL-H	double layer honeycomb
FGB	Function Cargo Block (from Russian Funktsionalno-gruzovoy blok)
HC	honeycomb
HITF	Hypervelocity Impact Technology Facility
ISS	International Space Station
JSC	Johnson Space Center
MMOD	micrometeoroid and orbital debris
NASA	National Aeronautics and Space Administration
NO	non optimum
PPI	pores per linear inch
SP	sandwich panel
WSTF	White Sands Test Facility

Notations

AD	Areal density
C	Coefficient
d	Projectile diameter (cm)
ρ	Density (g/cm^3)
K	Coefficient
K_{3s}	Low-velocity coefficient
K_{3d}	High-velocity coefficient
S	Overall spacing between outer bumper and rear wall (cm)
σ	Rear wall yield stress (ksi) (Note: 1 ksi = 1,000 lb/in^2 = 6.895 MPa)
t	Thickness (cm)
θ	Impact angle measured from normal to surface (degrees)
V	Projectile velocity (km/s)

Subscripts

c	critical
H	high
i	intermediate
L	low
n	normal
p	projectile
w	rear wall

Summary

The presence of a honeycomb core in a multi-wall shielding configuration for protection against micrometeoroid and orbital debris (MMOD) particle impacts at hypervelocity is generally considered to be detrimental as the cell walls act to restrict fragment cloud expansion, creating a more concentrated load on the shield rear wall. However, mission requirements often prevent the inclusion of a dedicated MMOD shield, and as such, structural honeycomb sandwich panels are amongst the most prevalent shield types. Open cell metallic foams are a relatively new material with novel mechanical and thermal properties that have shown promising results in preliminary hypervelocity impact shielding evaluations. In this study, an ISS-representative MMOD shielding configuration has been modified to evaluate the potential performance enhancement gained through the substitution of honeycomb for open cell foam. The baseline shielding configuration consists of a double mesh outer layer, two honeycomb sandwich panels, and an aluminum rear wall. In the modified configuration the two honeycomb cores are replaced by open-cell foam. To compensate for the heavier core material, facesheets have been removed from the second sandwich panel in the modified configuration.

A total of 19 tests on the double layer honeycomb and double layer foam configurations are reported. For comparable mechanical and thermal performance, the foam modifications were shown to provide a 15% improvement in critical projectile diameter at low velocities (i.e. 3 km/s) and a 3% increase at high velocities (i.e. 7 km/s) for normal impact. With increasing obliquity, the performance enhancement was predicted to increase, up to a 29% improvement at 60° (low velocity). Ballistic limit equations have been developed for the new configuration, and consider the mass of each individual shield component in order to maintain validity in the event of minor configuration modifications. Previously identified weaknesses of open cell foams for hypervelocity impact shielding such as large projectile diameters, low velocities, and high degrees of impact obliquity have all been investigated, and found to be negligible for the double-layer configuration.

Introduction

The performance of a dual-wall protective spacecraft structure against the impact of micrometeoroid and orbital debris (MMOD) particles is generally considered to be degraded by the presence of a honeycomb core. For impacts which penetrate the shield outer wall (bumper or front facesheet), projectile and bumper fragments disperse radially as they propagate through the shield interior, distributing the load over an area of the rear facesheet significantly larger than that of the original projectile diameter. The presence of honeycomb cell walls acts to restrict expansion, effectively channeling the fragments within a limited number of honeycomb cells for a more concentrated impact upon the rear facesheet. However, mission requirements often prevent the inclusion of a dedicated MMOD shielding structure, and as such, structural panels (i.e. honeycomb sandwich panels) also commonly serve as the protective system.

Metallic foams are a promising alternative to honeycomb structures as they offer comparable structural and thermal performance without the presence of MMOD shielding-detrimental channeling cells. In this report, modifications to a double-layer honeycomb sandwich panel shielding configuration representative of those used onboard the International Space Station (ISS) are evaluated.

Background

Hypervelocity Impact Performance of Honeycomb Sandwich Panels

Given their common application in space vehicle primary structures, the performance of honeycomb under impact of MMOD particles at hypervelocity has been investigated in a multitude of studies. Jex et al. [1] and Sibeaud et al. [2] discussed that the presence of a honeycomb core enhanced the shielding performance of a dual-wall structure at hypervelocity. They concluded that secondary impacts between ejecta fragments and cell walls overcompensated for the detrimental effect of channeling. A more commonly held view is that the presence of a honeycomb core is detrimental to the shielding performance. Taylor et al. [3] quantified the degradation in performance through inclusion of a scaling factor which acts to reduce the effective rear facesheet thickness by 50% in definition of the panel ballistic limit at hypervelocities (i.e. molten and/or vaporized ejecta). Ryan et al. [4] defined a degradation in shielding performance due to the presence of a honeycomb core equal to a ~46% reduction in shielding capability at normal impact, reducing with increasing obliquity (e.g. for impact at 60°, the degradation in performance drops to ~18%). Sennett and Lathrop [5] also quantified the effect of the honeycomb core, stating that once the panel thickness increases above two times the honeycomb cell size, no increase in shielding capability is achieved with an increase in shield thickness when fragments were either molten or vaporized. For solid fragment ejecta, the effect was not nearly as severe. In Figure 1 a comparison between the rear wall thickness for a dual-wall shield with and without a honeycomb core, required to defeat a design projectile, is shown. For the Whipple shield configuration (i.e. no honeycomb core), the inverse-square root relationship of Cour-Palais [6] for the non-optimum condition is used.

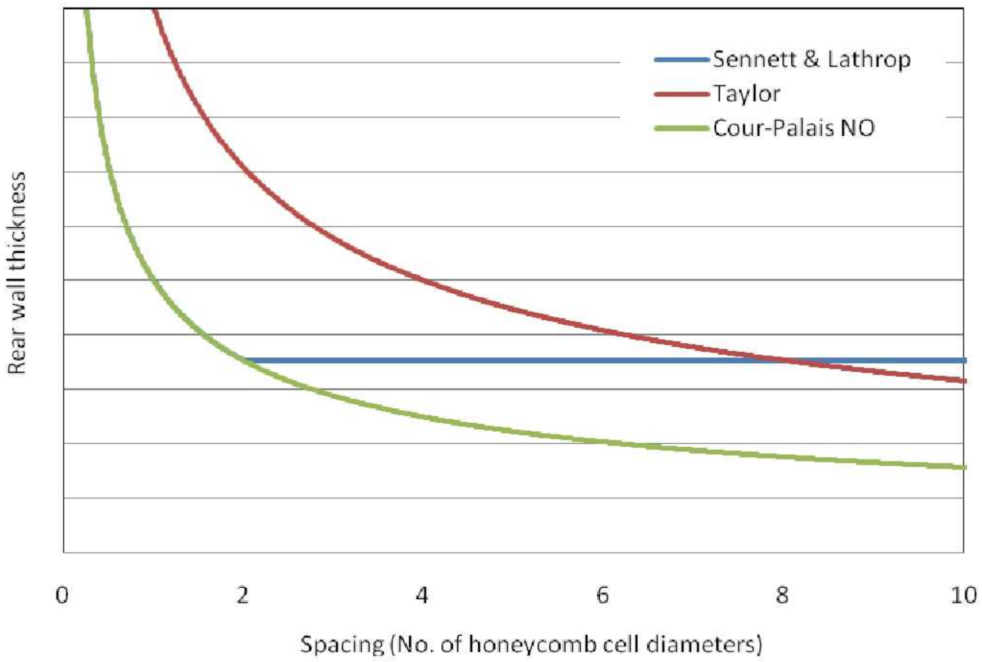

Figure 1: Rear wall sizing for a dual-wall shield with (Sennett & Lathrop, Taylor) and without (Cour-Palais NO) a honeycomb core.

At oblique angles of impact, the presence of honeycomb cell walls increase the amount of shielding material "seen" by the impacting projectile. Thus, the dependency of shielding capability on impact angle is greater for honeycomb sandwich panels than equivalent Whipple shields (i.e. an increase in impact angle increases the shielding performance of honeycomb sandwich panels more than that of the equivalent Whipple shield). The damage induced in honeycomb cores when subject to oblique hypervelocity impact can be differentiated between that caused by an ejecta cone normal to the structure surface, and that along the line of the projectile velocity vector (see Figure 2 for example). For space-representative sandwich panels, the ballistic limit is nearly always defined by the onset of perforation induced by the ejecta cone normal to the facesheet surface. For impact conditions marginally above the ballistic limit, fragments propagating along the projectile velocity vector are defeated within the honeycomb core. As the projectile kinetic energy is increased and the panel is more significantly damaged, the velocity vector fragments travel deeper within the honeycomb core until the impact kinetic energy is sufficiently high that they are able to penetrate the sandwich panel rear facesheet. For some configurations, separate perforation holes can be produced relating to the debris ejected at normal incidence to the front facesheet and the projectile velocity vector, an example of which is shown in Figure 3.

Hypervelocity Impact Performance of Metallic Open-Cell Foams

Preliminary investigations of the hypervelocity impact performance of metal foam structures have demonstrated their potential, particularly in comparison with traditional structural panels. In [7] alternative configurations for the ISS Columbus module shielding were evaluated. One of the configurations included a panel of open-cell aluminum foam, referred to AB2Mod. A schematic of the AB2Mod shield is provided in Figure 4.

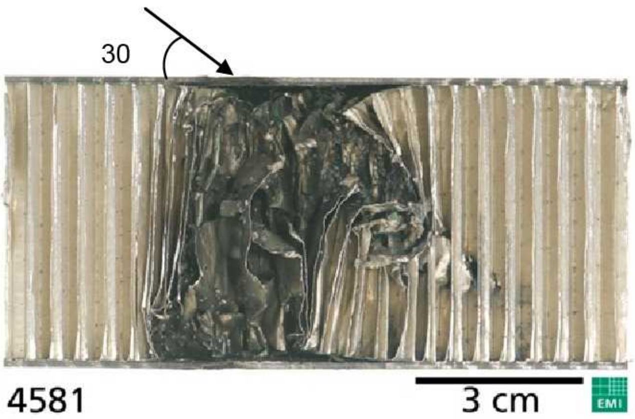

Figure 2: Internal honeycomb damage following impact of a 3.0 mm diameter 99.9% Al-sphere at 60° with a velocity of 6.29 km/s.

Figure 3: Damage to a sandwich panel with 1.37mm thick CFRP facesheets and a 25mm thick 3/16-5056-.001 honeycomb core impacted at 60° by a 3.0mm Al99.9% projectile at 6.29 km/s. Left: Front facesheet damage; Right: Rear facesheet damage showing two perforation holes related (1) to the debris ejected at normal incidence to the front facesheet and (2) along the projectile velocity vector.

Testing found that the AB2Mod configuration provided increased protection over the reference Columbus stuffed Whipple shield at high velocities (> 6 km/s) and normal incidence. At oblique incidence, the performance of the reference stuffed Whipple shield and foam-modified configuration were comparable (at high velocity). For low velocity testing, the performance of the AB2Mod configuration was clearly worse than that of the reference Columbus shield. The authors concluded that the foam configuration was vulnerable to impact of large projectiles (above 1 cm in diameter) at low velocities, as the shield was unable to induce projectile fragmentation. The authors note that while the foam configuration provided a similar level of protection to the reference stuffed Whipple shield overall, the primary advantages of the configuration are related to the extension of the area of the pressure shell that can be protected (due to a concentration of mass in the outer layer), and to other design aspects such as a reduction in non-ballistic mass (stiffeners, local reinforcements, etc.).

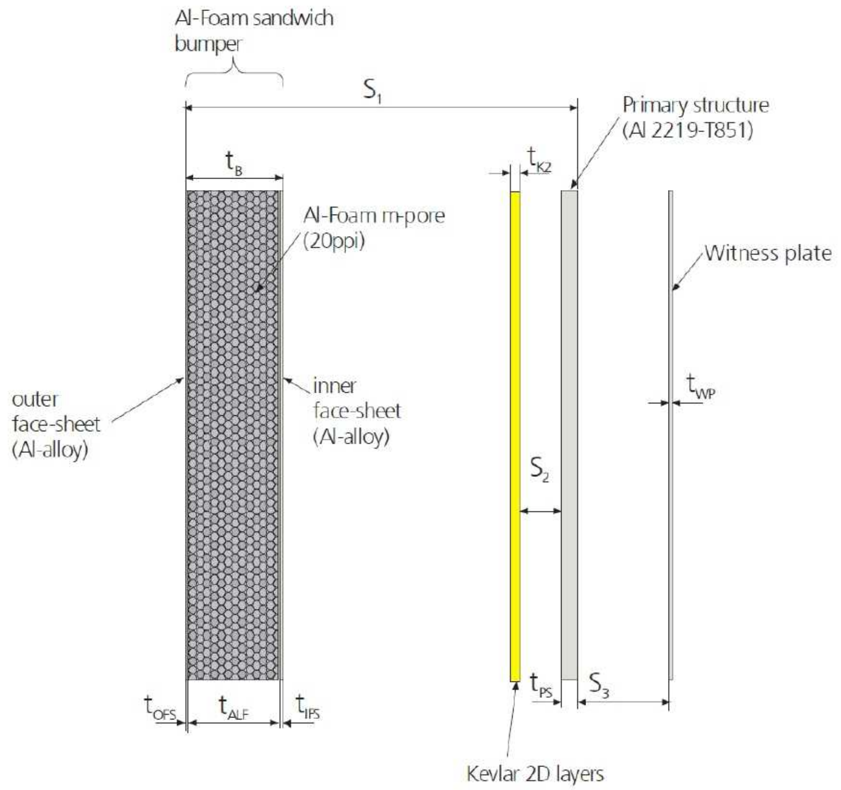

Figure 4: Alternate Columbus MMOD shield configuration incorporating metallic open-cell foam (from [7]).

The shielding performance of sandwich panel structures with open-cell aluminum foam cores was evaluated in [8] against that of aluminum honeycomb core sandwich panels (Al HC SP). In Figure 5, a comparison between the damages induced by the impact of 3.6 mm Al 2017-T4 spheres at normal incidence with velocities of 6.49±0.27 km/s on 5.08 cm thick sandwich panels is shown. It should be noted that the facesheets of the honeycomb sandwich panel were significantly thicker than those of the foam sandwich panel (0.127 cm vs 0.0254 cm) in order to provide comparable areal densities.

In Figure 5 the foam core is shown to restrict fragment radial expansion to an equal or greater degree than the honeycomb. However, while fragments are expected to be channeled within the honeycomb cells, the foam homogeneity should ensure that resistance to fragment cloud expansion is equal in all directions, therefore limiting the degree of channeling. Damage to the sandwich panel rear facesheets in this example demonstrates the potential improvements in hypervelocity shielding performance to be gained through the replacement of honeycomb cores with open-cell foams.

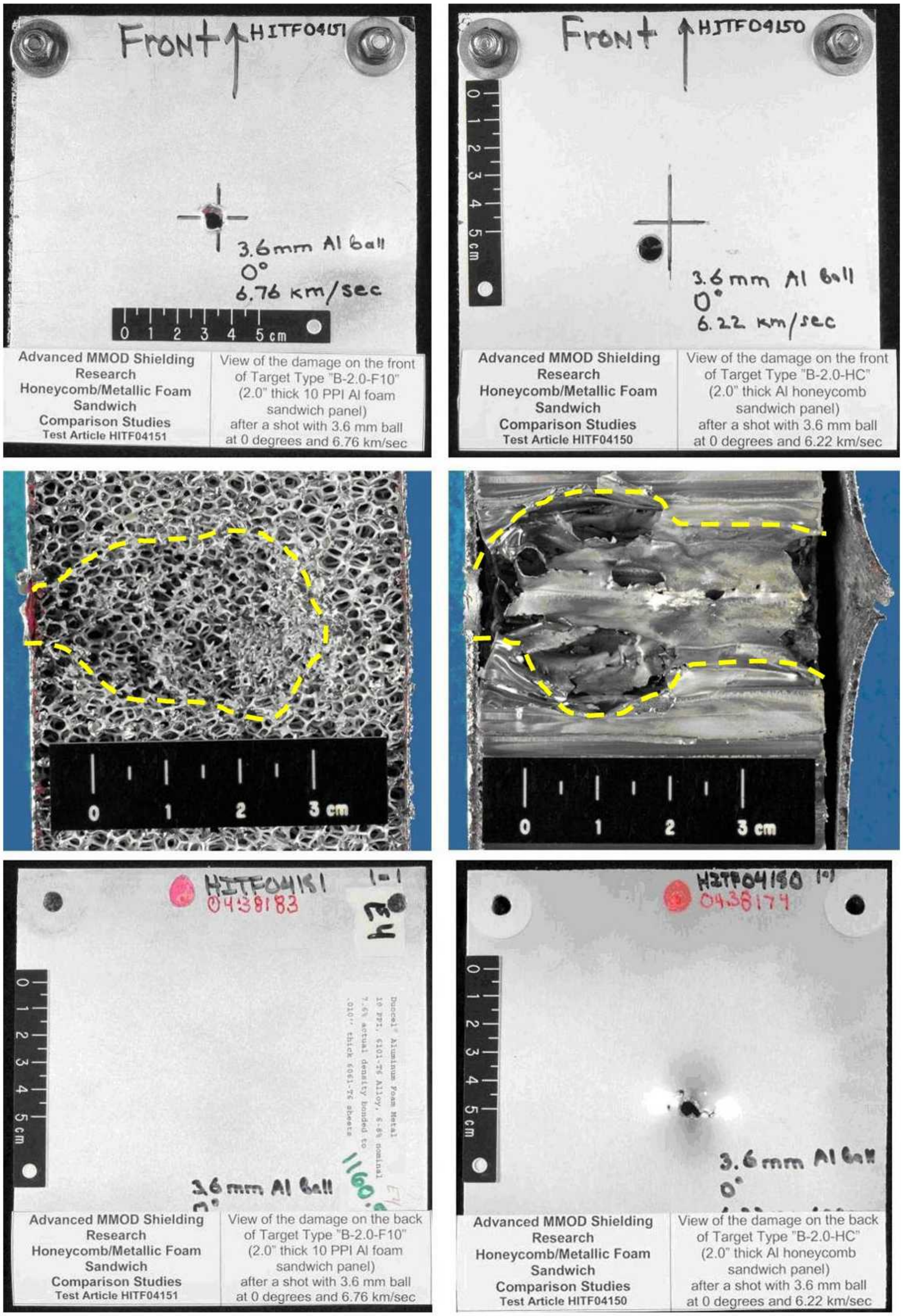

Figure 5: Comparison of damages in a open cell foam core (left) and honeycomb core (right) sandwich panel structures impacted by a 3.6 mm Al-sphere at 6.49±0.27 km/s (0°). Upper: front facesheet damage; Middle: core damage (sectioned); Bottom: rear facesheet damage. (from [8]).

Definition and Properties of Aluminum Open-Cell Foam

Open cell foam is specified in terms of core density relative to the base material (%), and pore density in terms of pores per linear inch (PPI). In Figure 6 foam cells and pores are defined. Foam cells are typically 14-faceted polyhedral or solid tetrakaidecahedrons, while pores are the individual windows between the interconnected foam ligaments.

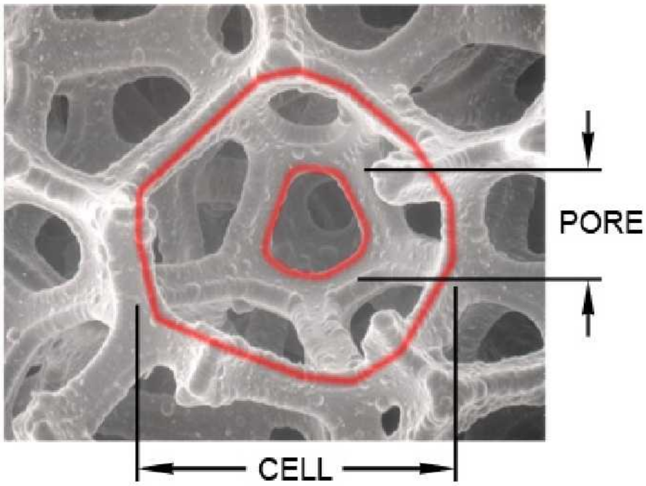

Figure 6: Definition of open cell foam pore and cell size (© ERG Aerospace).

While pore density controls the number and nominal size of foam ligaments, the relative density controls their cross-sectional form and actual size, see Figure 7.

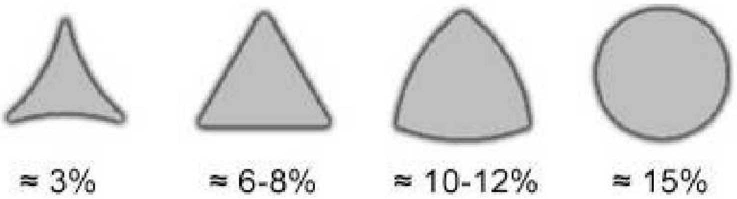

Figure 7: Ligament cross section shape variation with relative density (© ERG Aerospace).

Depending on manufacturing technique, the mechanical performance of metallic open-cell foams can vary widely. For foams formed through utilization of a solid negative-image ceramic mould (such as the Duocel foam manufactured by ERG Aerospace), the mechanical properties of the final product can be approximated by the base material properties and the foam relative density (ρ_{rel}), i.e. for Young's modulus (E) and crush strength (σ):

$$E_{foam} = E_{mat} \cdot \rho_{rel}^{2} \tag{1}$$

$$\sigma_{foam} = C_1 \cdot \sigma_{mat} \cdot \rho_{rel}^{3/2} \tag{2}$$

where $C_1 = 0.3$ for a wide variety of foams [9]

Target Description

Double Layer Honeycomb (DL-H)

The baseline target is representative of that used on the FGB end cone and is shown in Figure 8.

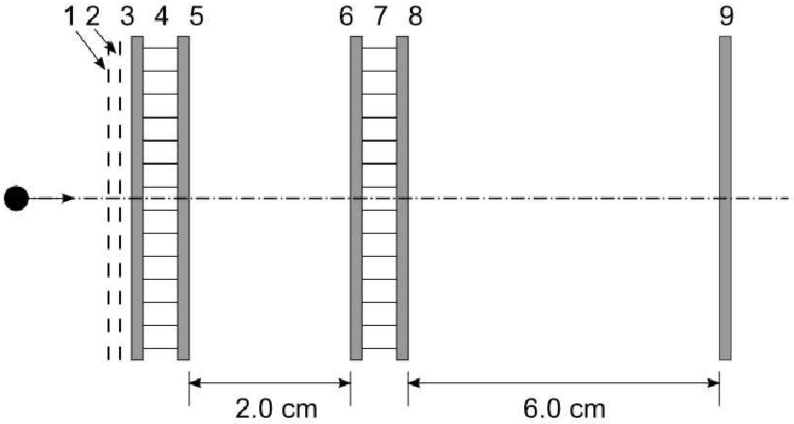

Figure 8: Schematic of the double layer honeycomb target configuration.

A description of the target components is given in Figure 8. The total areal density of the double honeycomb configuration is 1.57 g/cm^3.

Table 1: Description of double layer honeycomb target components.

	Description	Designation	Thickness (mm)	Areal density (g/cm^2)
1	Mesh outer layer	30×30* SS304 mesh (∅ = 0.016”)	0.457	0.20
2	Mesh inner layer	30×30* SS304 mesh (∅ = 0.016”)	0.457	0.20
3	SP1 front facesheet	Al6061-T6	0.4064	
4	SP1 honeycomb core	1.8-5052-.002	12.7	0.37
5	SP1 rear facesheet	Al6061-T6	0.4064	
6	SP2 front facesheet	Al6061-T6	0.4064	
7	SP2 honeycomb core	1.8-5052-.002	12.7	0.37
8	SP2 rear facesheet	Al6061-T6	0.4064	
9	Real wall	Al2024-T3	1.016	0.43

* 30 indicates the number of openings per linear inch in the mesh

Double Layer Foam (DL-F)

The double layer foam target replaces the two honeycomb sandwich panels of the baseline target with 12.7 mm thick open cell Al6101-T6 foam sandwich panels manufactured by ERG Aerospace. As the areal weight of the foam core (6-8% relative density) is greater than the honeycomb (~4.8%), facesheets are only installed on the front foam panel. The foam has a pore density of 10 per linear inch (PPI), details of which are given in Figure 9.

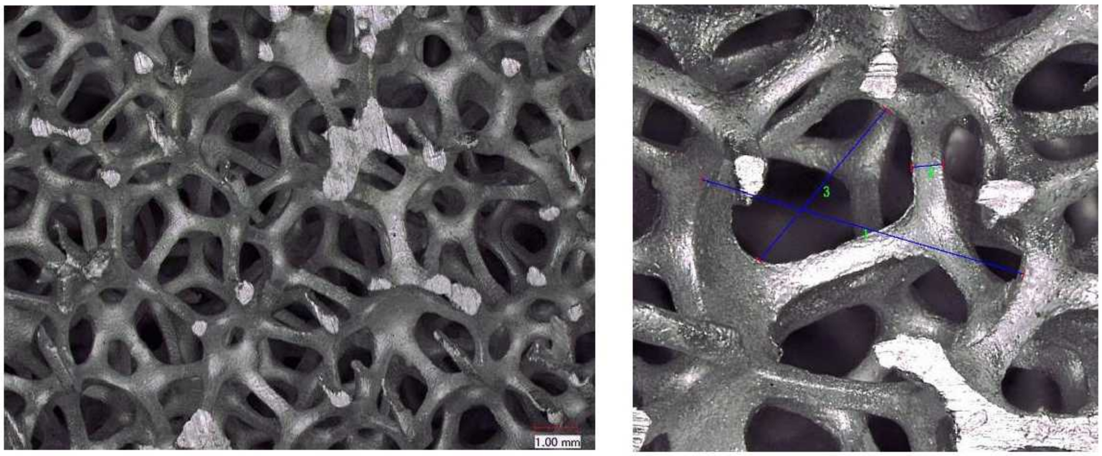

Figure 9: Characterization of the 10 PPI foam structure. Cell size (1) = 3.95 mm, pore size (3) = 2.33 mm, ligament width (2) = 382 μm.

A schematic of the double layer foam target is shown in Figure 10.

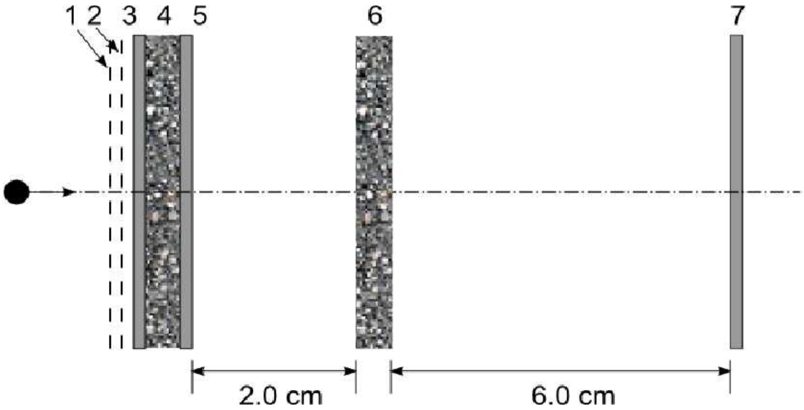

Figure 10: Schematic of the double layer foam target configuration.

A description of the target components is given in Table 2. The total areal density of the double foam configuration is 1.68 g/cm^2.

Table 2: Description of double layer honeycomb target components.

	Description	Designation	Thickness	Areal density
1	Mesh outer layer	30×30* SS304 mesh	0.457 mm	0.20 g/cm^2
2	Mesh inner layer	30×30* SS304 mesh	0.457 mm	0.20 g/cm^2
3	SP1 front facesheet	Al6061-T6	0.4064 mm	
4	SP1 foam core	10 PPI Al6101-T6 foam	12.7 mm	0.56 g/cm^2
5	SP1 rear facesheet	Al6061-T6	0.4064 mm	
6	Foam panel	10 PPI Al6101-T6 foam	12.7 mm	0.29 g/cm^2
7	Real wall	Al2024-T3	1.016 mm	0.43 g/cm^2

Test Results

A series of 19 hypervelocity impact tests were performed on the double layer targets, 13 on the foam configuration and six on the honeycomb configuration. A summary of the test conditions and results are presented in Table 3.

Table 3: Hypervelocity impact test results.

	Reference	Target	Angle (deg)	Projectile		Impact Velocity (km/s)	Result (P/SP/NP)
				Material	Diameter (cm)		
1	HITF08592	DL-F	0	Al2017-T4	0.877	6.76	NP
2	HITF08593	DL-F	45	Al2017-T4	0.837	6.87	NP
3	HITF08594	DL-F	60	Al2017-T4	1.114	66.9	P
4	HITF08595	DL-F	0	Al2017-T4	0.717	3.29	P
5	HITF08599	DL-F	60	Al2017-T4	1.005	7.03	P
6	HITF08596	DL-F	0	Al2017-T4	0.637	3.67	P
7	HITF08597	DL-F	45	Al2017-T4	0.662	3.68	NP
8	HITF08598	DL-F	45	Al2017-T4	0.837	3.62	NP
9	HITF09024	DL-F	60	Al2017-T4	1.005	6.80	NP
10	HITF09038	DL-F	60	Al2017-T4	1.115	6.69	NP
11	HITF09064	DL-F	60	Al2017-T4	1.276	7.00	SP
12	HITF07460	DL-F	0	Al2017-T4	0.833	6.74	NP
13	HITF07461	DL-F	45	Al2017-T4	0.873	6.89	P
14	HITF07458	DL-H	45	Al2017-T4	0.754	6.94	NP
15	HITF07459	DL-H	45	Al2017-T4	0.650	6.88	NP
16	HITF07504	DL-H	0	Al2017-T4	0.730	6.86	NP
17	HITF07509	DL-H	0	Al2017-T4	0.754	6.93	NP
18	HITF07510	DL-H	45	Al2017-T4	0.873	6.74	P
19	HITF07629	DL-H	0	Al2017-T4	0.833	6.91	P

Evaluation of Shield Modification

In order to evaluate the effect of interchanging aluminum honeycomb for open-cell aluminum foam in the double-layer shielding configuration, a direct comparison can be made between impact damages induced on both configurations at nominally-identical impact conditions. In Figure 11 damages induced in the DL-H and DL-F targets by the impact of 0.833 cm diameter projectiles at 6.83±0.09 km/s with normal incidence are compared. Damage in the two mesh layers, and the entry hole on the 1st sandwich panel are similar for both configurations. The diameter of rear facesheet material peeled back from the 1st sandwich panel exit hole is also similar; however the extension of core damage is noticeably less in the foam sandwich panel. The through hole in the 2nd panels is shown to be significantly larger for the DL-H configuration than the DL-F shield (88×90 mm vs. 70×62 mm), indicating that the debris cloud is more finely concentrated by the foam sandwich panel bumper than the honeycomb sandwich panel. The rear wall of the DL-H configuration is perforated, showing a large through crack (80 mm in length, 5 mm wide) and multiple individual craters (multiple small bulges observable on the rear side of the panel). Given the appearance of the through crack, it is expected that failure of the rear wall occurred through penetration of individual solid fragments which acted as crack initiation sites that were propagated during the impulsive load of the fragment cloud. The rear wall of the DL-F configuration is significantly deformed, yet there is no perforation or detachment of spalled material from the rear surface. The majority of deposits on the rear wall are from molten aluminum, resulting in the bright silver coating that can be observed in the target photograph. The rear wall shows some cratering from impact of individual solid fragments, which are also visible as small dimples on the rear side of the panel. Under these impact conditions, the performance of the DL-F shield is clearly superior to that of the baseline DL-H shield.

In Figure 12 damages induced in the two configurations under oblique (45°) impact of 0.873 cm diameter projectiles at 6.81±0.08 km/s are compared. In the two outer mesh layers the damage is similar. The entry hole in the 1st foam sandwich panel is slightly larger than that of the HC SP (28×29 mm vs. 23×26 mm), however the profile of the entry holes are similar in appearance. The exit hole in the 1st foam sandwich panel is round, offset from the entry hole in the direction of the projectile flight vector. The damage to the panel rear facesheet is significantly larger than that in the foam core (due to delamination), similar to the 0° test. For the honeycomb sandwich panel, the exit hole is circular in shape, however the petals to the upper left of the exit hole are not fully folded back, giving the hole an unusual shape. The honeycomb core damage limits correspond to the rear facesheet damage extension, and are again significantly larger than that in the foam core. The through holes in the 2nd panels are more similar in size than the 0° test, however the HC SP hole diameter is still larger than the foam panel. For the HC SP, the rear facesheet petals are peeled back beyond the extension of honeycomb core damage. Both shield rear walls are perforated, with multiple small perforation and spallation sites most likely from individual solid fragments. The DL-F rear wall is more significantly deformed than the DL-H panel, and shows clear deposits of melted aluminum.

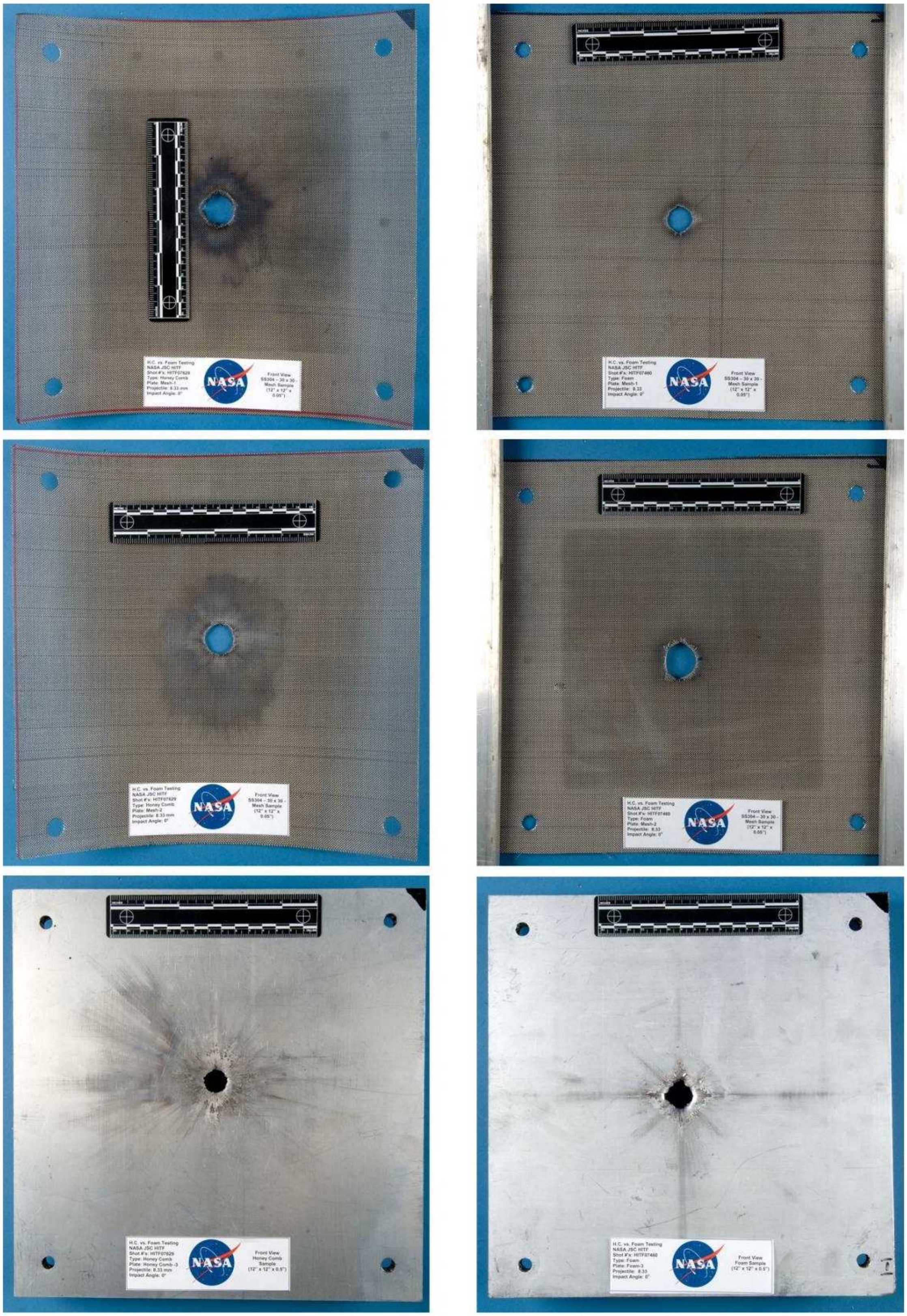

Figure 11: Comparison of impact damages in the DL-H (left) and DL-F (right) targets impacted by a 0.833 cm diameter Al 2017-T4 sphere at 6.83±0.09 km/s and 0°. From top to bottom: 1st mesh layer (front view), 2nd mesh layer (front view), 1st sandwich panel (front view).

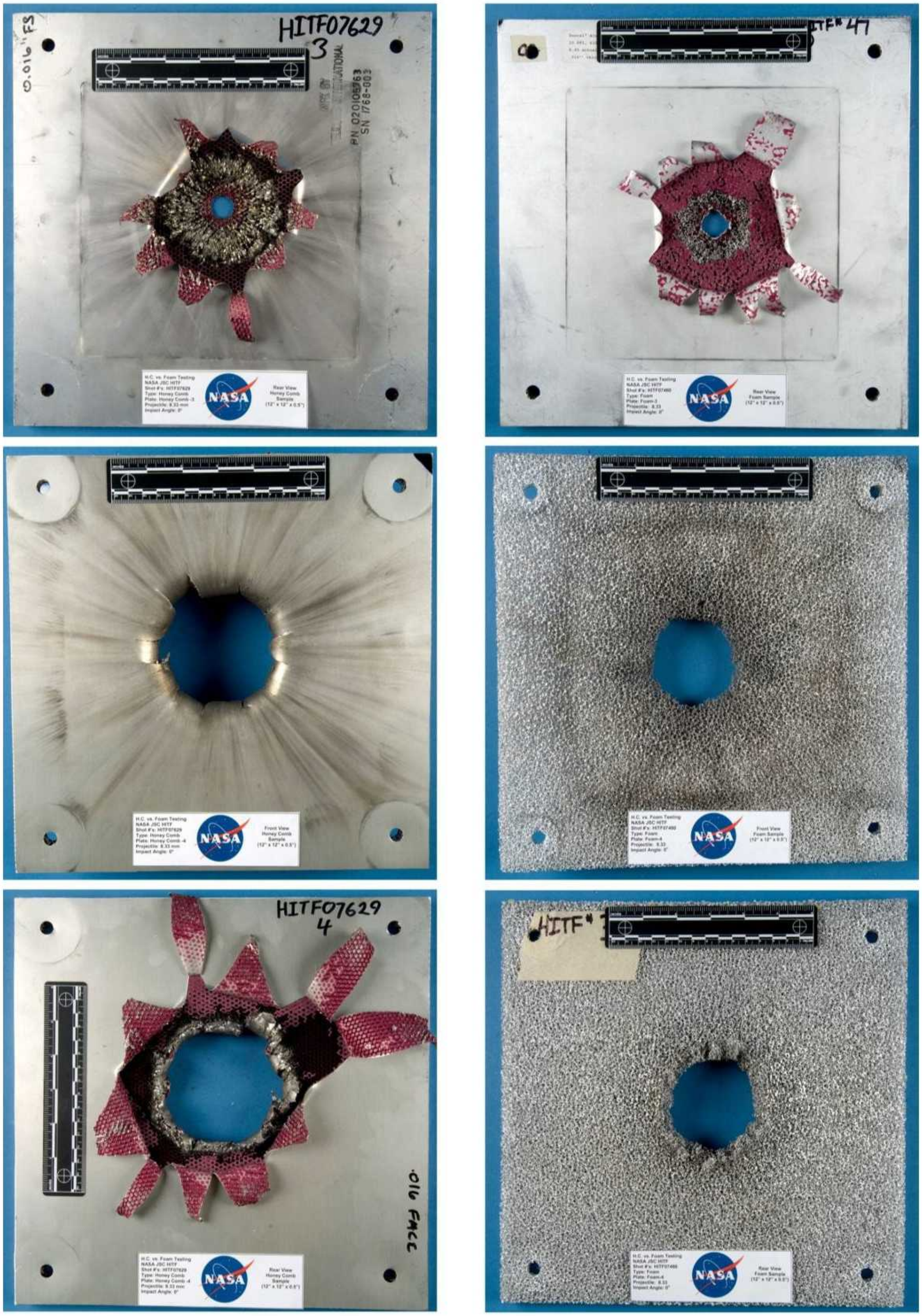

Figure 11 (cont): Comparison of impact damages in the DL-H (left) and DL-F (right) targets impacted by a 0.833 cm diameter Al 2017-T4 sphere at ~6.83±0.09 km/s and 0°. From top to bottom: 1st sandwich panel (rear view), 2nd sandwich panel (front view), 2nd sandwich panel (rear view).

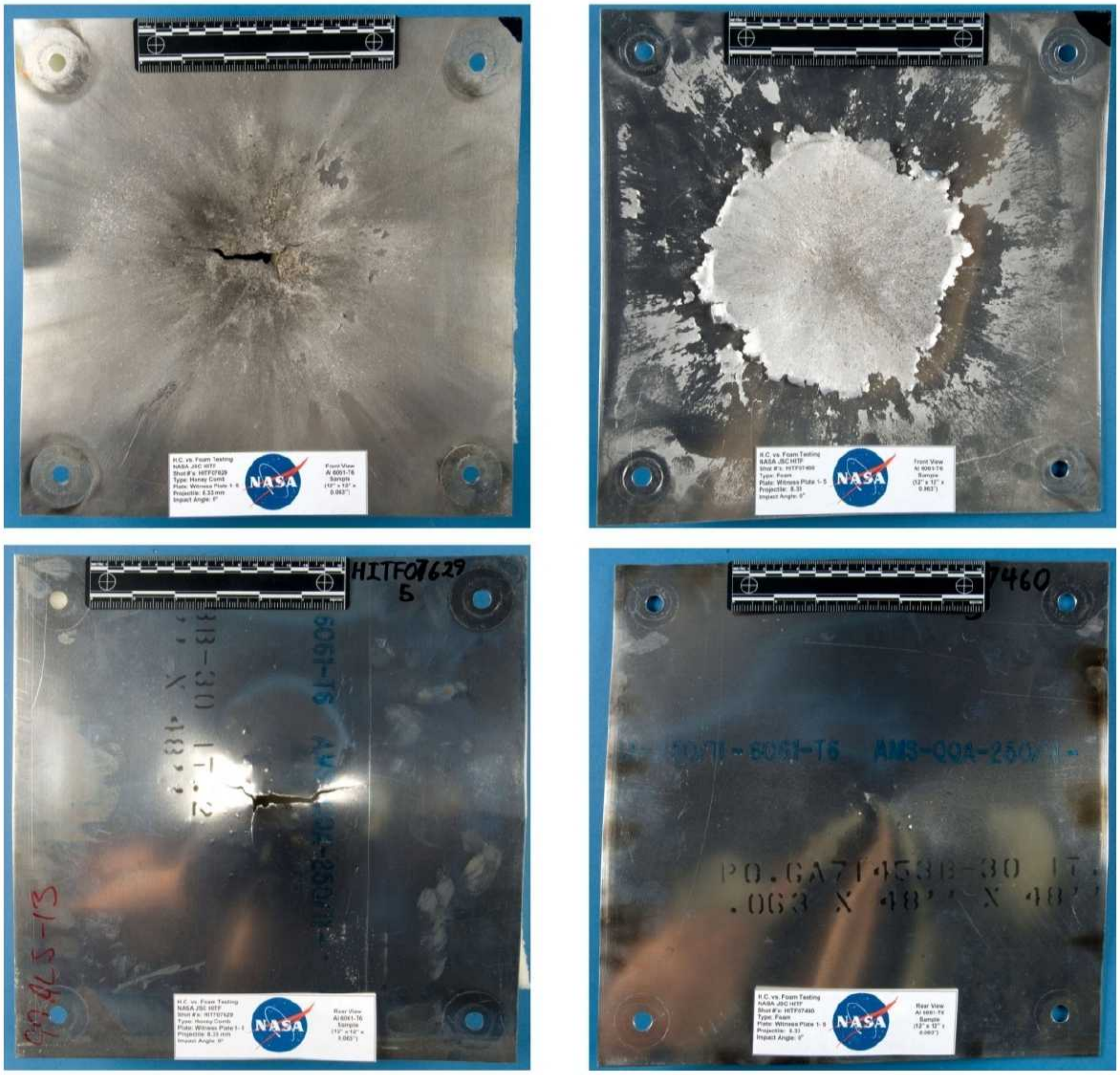

Figure 11 (cont): Comparison of impact damages in the DL-H (left) and DL-F (right) targets impacted by a 0.833 cm diameter Al 2017-T4 sphere at 6.83±0.09 km/s and 0°. From top to bottom: rear wall (front view), rear wall (rear view).

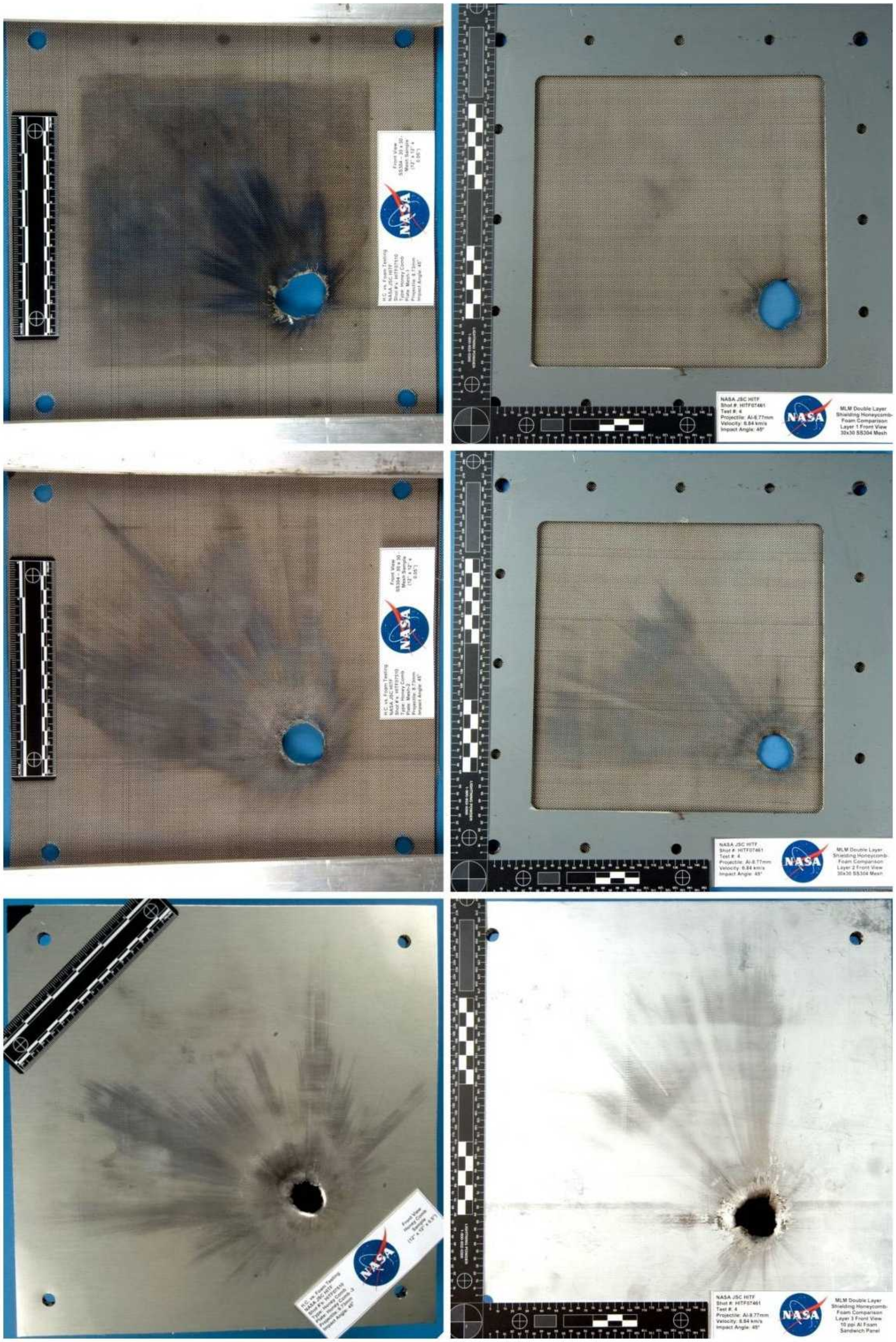

Figure 12: Comparison of impact damages in the DL-H (left) and DL-F (right) targets impacted by a 0.873 cm diameter Al 2017-T4 sphere at 6.81±0.08 km/s and 45°. From top to bottom: 1st mesh layer (front view), 2nd mesh layer (front view), 1st sandwich panel (front view).

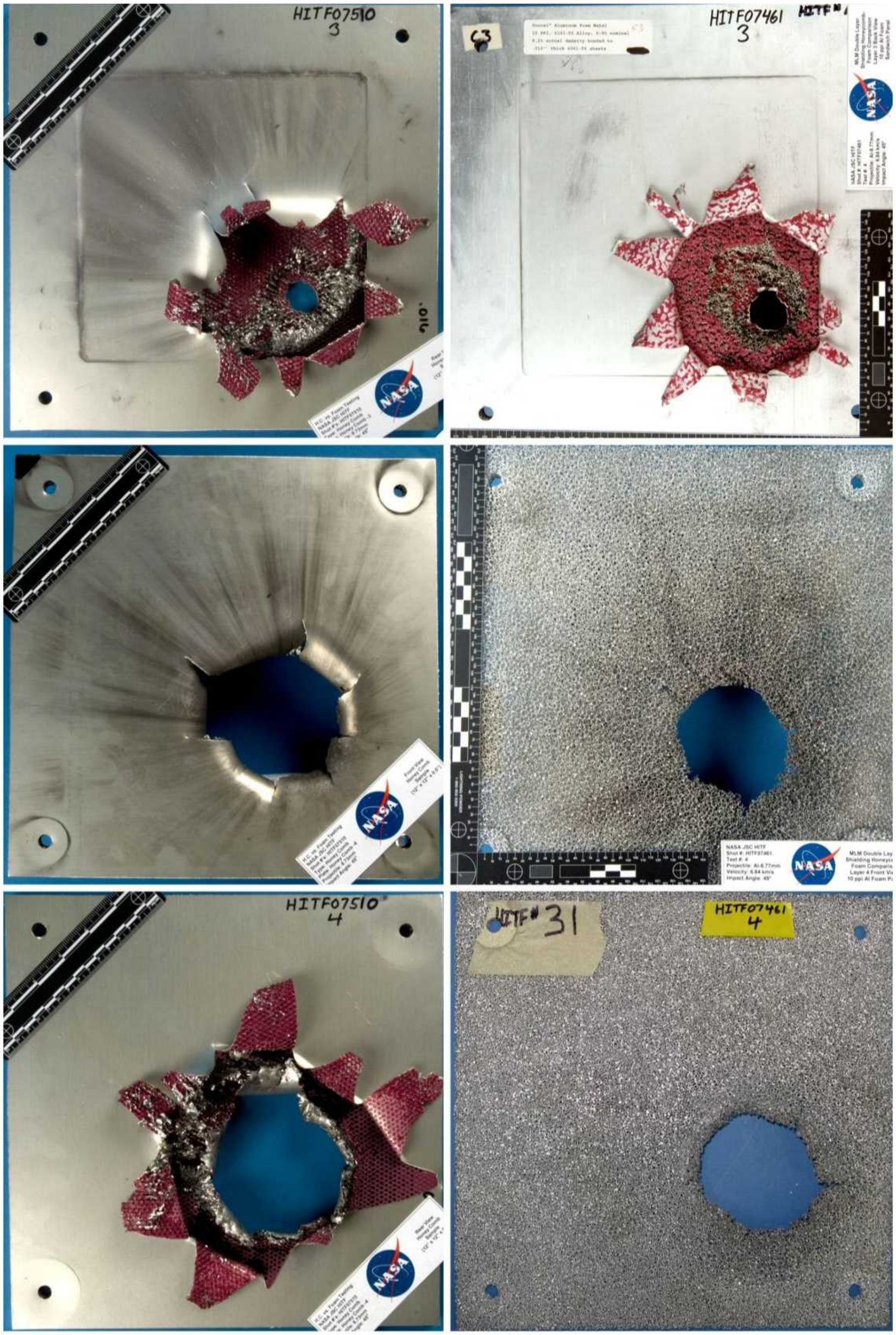

Figure 12 (cont.): Comparison of impact damages in the DL-H (left) and DL-F (right) targets impacted by a 0.873 cm diameter Al 2017-T4 sphere at 6.81±0.08 km/s and 45°. 1st sandwich panel (rear view), 2nd sandwich panel (front view), 2nd sandwich panel (rear view).

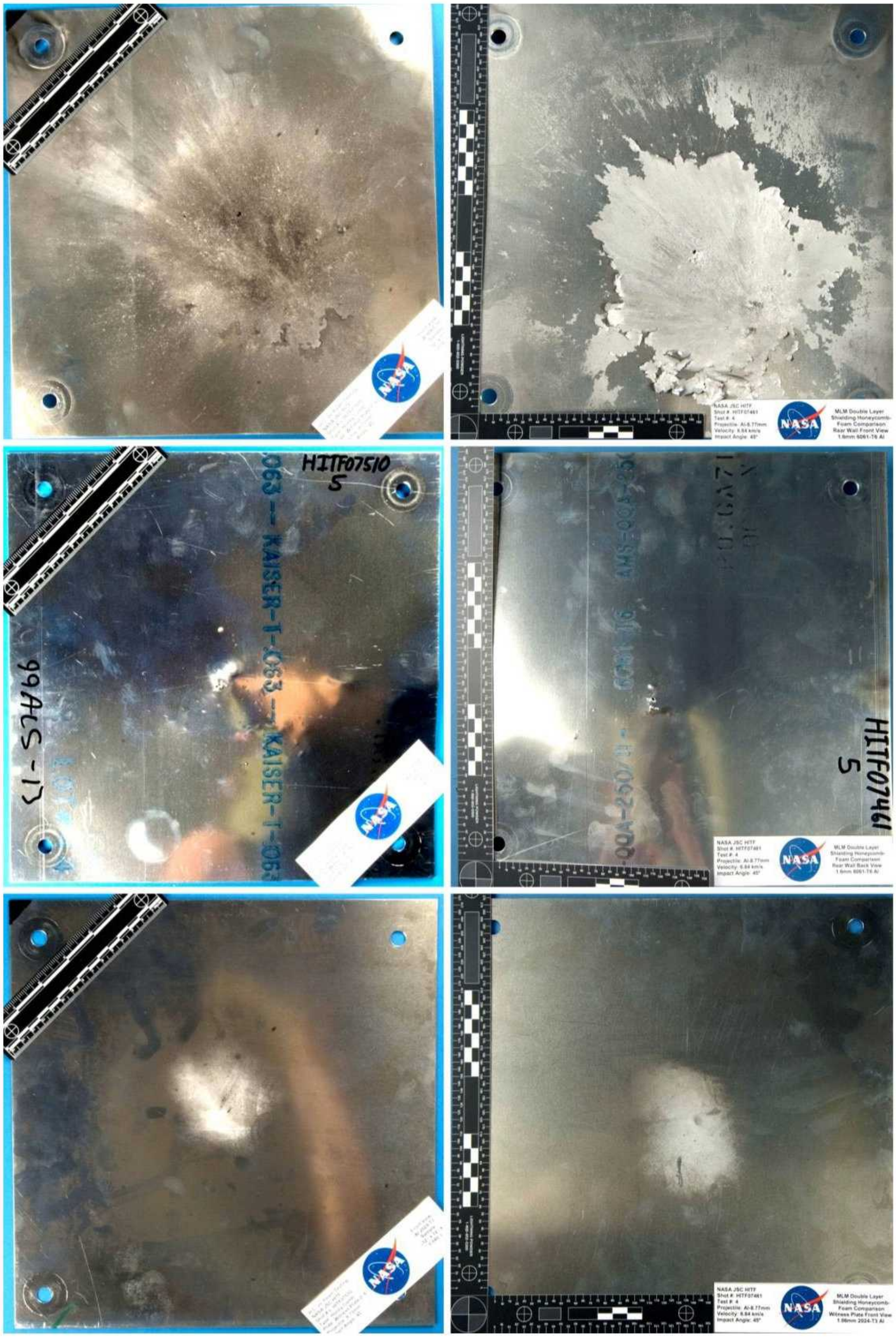

Figure 12 (cont.): Comparison of impact damages in the DL-H (left) and DL-F (right) targets impacted by a 0.873 cm diameter Al 2017-T4 sphere at 6.81±0.08 km/s and 45°. From top to bottom: rear wall (front view), rear wall (rear view), witness plate (front view).

The Effect of Impact Angle on Shield Performance

In Figure 13 a comparison between rear wall damage for the DL-H target impacted by 0.754 cm diameter projectiles at ~6.9 km/s with normal (0°, HITF07509) and oblique (45°, HITF07458) incidence is shown. The shield rear wall was not perforated in either test, however the degree of damage to the 45° test is noticeably less than the normal incidence test. At 0° the front side of the rear wall shows more deposits and a number of craters in the central damage zone. Also, the plate is significantly deformed, while the rear wall from the 45° test has minimal bulging/deformation. It is considered that the 0° target is very close to the limit of perforation.

Figure 13: Comparison of impact damages in the DL-H target rear wall impacted by 0.754 cm diameter Al 2017-T4 spheres at ~6.9 km/s with normal (left) and oblique (45°, right).

In Figure 14 a comparison between rear wall damage for the DL-F target impacted by 1.005 cm diameter projectiles at ~6.9 km/s is shown. For impact at 30° (HITF08599), the rear wall is severely perforated, showing a large petalled perforation hole and extensive cracking. The front of the panel shows extensive deposits of melted aluminum and some cratering about the jagged hole edges. From the appearance of the petalled edges it is considered that the rapid hole growth was initiated by perforation of solid individual fragments. The subsequent deformation of the petals and entire panel resulted from impulsive loading of the predominantly molten fragment cloud. For impact at 60° (HITF09024) the rear wall is not perforated, and is significantly less deformed than the structure impacted at 30°. The front side of the rear wall shows considerable deposits of melted aluminum and a small degree of cratering spread throughout the damage zone. Normal to the impact site there are deposits of solid foam fragments upon the rear wall, most likely from the slower moving outer edges of the fragment cloud. The target is well below the ballistic limit for this impactor at 60°, indicating a clear enhancement in shielding performance with increasing obliquity.

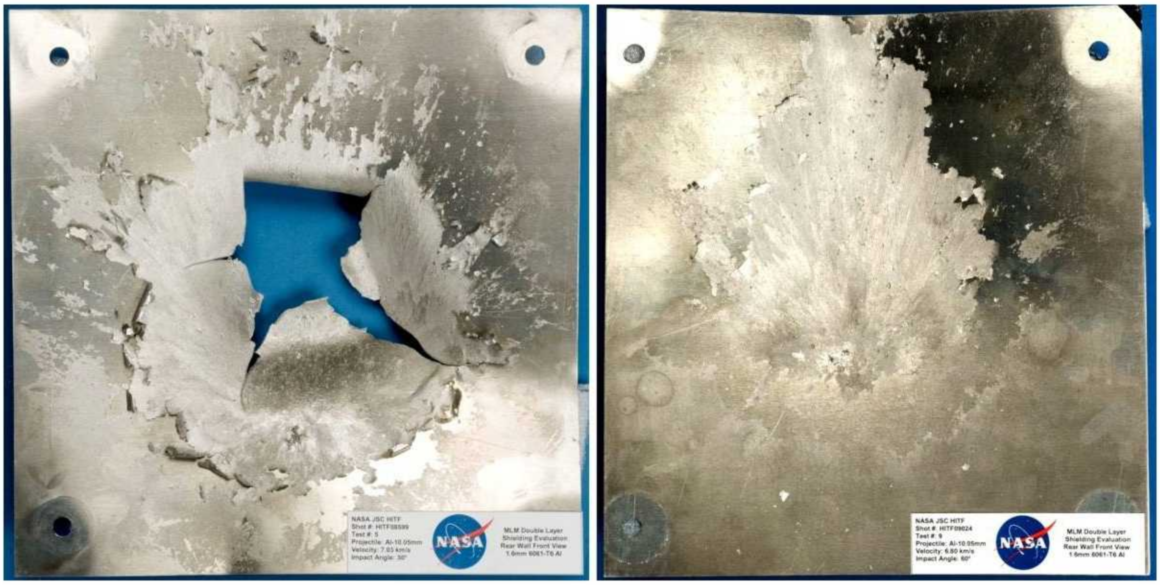

Figure 14: Comparison of impact damages in the DL-F target rear wall impacted by 1.005 cm diameter Al 2017-T4 spheres at ~6.9 km/s with oblique incidence. Left: 30°, right: 60°.

Low Velocity Shield Performance

One of the promising shielding mechanisms of open-cell metallic foam is the effect of secondary impacts by projectile and bumper fragments upon individual foam cell ligaments. By repeatedly shocking these fragments, it is expected that increased fragmentation and melting can be achieved at lower velocities than for conventional shielding configurations (e.g. Whipple shield, honeycomb sandwich panel). In Figure 15 the rear wall of a DL-F configuration impacted at 3.29 km/s is shown with clear deposits of melted aluminum.

Figure 15: Melted aluminum deposits and solid fragment damage of the DL-F rear wall impacted by a 0.717 cm diameter projectile at 3.29 km/s with normal incidence (HITF08595).

Although there is no impact data for the DL-H configuration at impact speeds below 6.74 km/s it is still possible to identify the effect of secondary impacts upon the foam structure, compared to that resulting from impacts upon the target intermediate layers. The multi-shock shield [10] utilized repeated shocking of projectile fragments to increase the degree of projectile fragmentation and melting. If the core structures are neglected, the configurations evaluated in this study are basically inefficiently spaced metallic multi-shock shields with a double mesh outer layer. All-metal multi-shock shields were shown in [10] to produce rear wall damage characteristics for normal impact at 6.3 km/s representative of those at 10 km/s on a single bumper shield configuration.

Figure 16 shows rear wall damage for the DL-H and DL-F configurations impacted at 6.91 km/s and 6.74 km/s respectively. The DL-F target shows a degree of melted aluminum deposits, although the predominant damage feature is cratering about the central damage zone. Alternatively, the DL-F target shows significant deposits of melted aluminum over a large central area with only a small number of finite craters. Clearly, therefore, secondary impacts on the foam ligaments act to increase the degree of projectile fragmentation, melting and vaporization at lower impact velocities beyond that of the DL-H configuration.

Alme et al. [ref] calculated the effect of multiple impact shocks on projectile internal energy, finding that the non-isentropic shock and release process resulted in an increase in projectile entropy (or internal energy). Thus, the limit conditions determined by Swift [11] for melt and vaporization of metallic projectiles based on the concept of entropy trapping in which the entropy injected into projectile and target materials can be calculated from the Hugoniot and release isentrope, can be reached by a multi-bumper shield at lower impact velocities than a single bumper configuration. As noted previously, there is clear evidence of projectile melting below 3.29 km/s for the DL-F configuration.

A Ballistic Limit for the Double-Layer Foam Shield Configuration

The baseline double-layer honeycomb shield is representative of the enhanced zone 11 shield onboard the FGB module of the ISS [12]. For FGB shielding a generic ballistic limit equation was defined, based on the JSC Whipple Shield equation [13]. In order to adjust the equation to suit the double-layer honeycomb configuration the bumper thickness was estimated using the areal density of the 1st honeycomb layer, and half the density of the 2nd honeycomb layer. The remaining 50% of the 2nd honeycomb layer was added to the thickness of the shield rear wall. Secondly, impact testing was performed to provide an empirical basis for adjusting the equation constants.

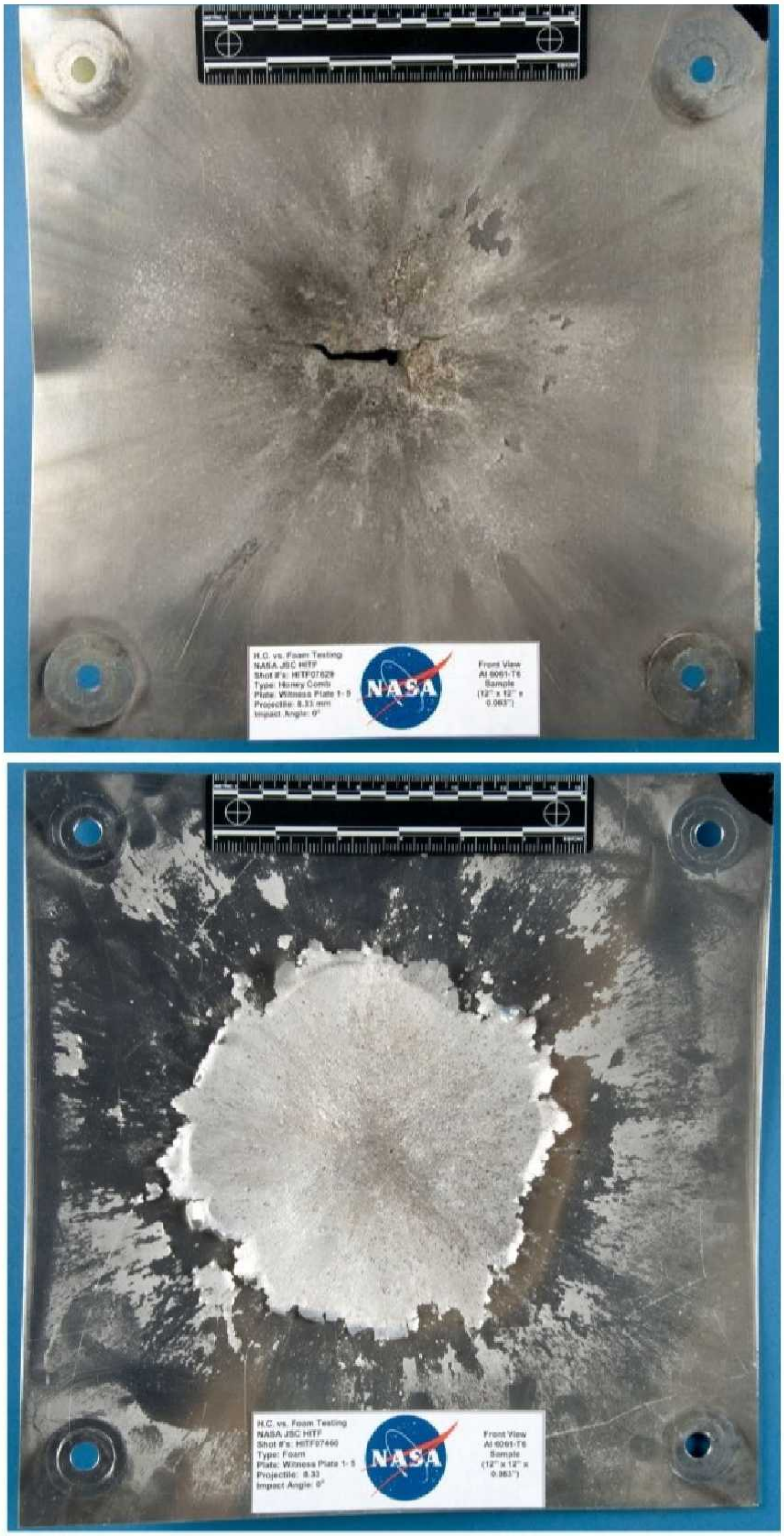

Figure 16: Demonstrating the effect of the foam microstructure on projectile fragmentation and melt. Rear wall damage for the DL-H (upper) and DL-F (lower) shields impacted by 0.833 cm diameter projectiles at ~6.9 km/s and 0°.

The general FGB ballistic limit equation (repeated from [12]) is defined as:

High velocity: when $V \geq V_H/\cos\theta$,

$$d_c = C_H \left(V \cos\theta\right)^{-2/3} \rho_p^{-1/3} \tag{3}$$

where V – Projectile velocity (km/s)
V_L – Low velocity regime upper limit (km/s)
d_c – Critical projectile diameter (cm)
C_H – High velocity fit coefficient (-)
θ – Impact angle (deg)
ρ_p – Projectile density (g/cm^3)

Intermediate velocity: when $V_L/\cos\theta > V > V_H/\cos\theta$,

$$d_c = C_h \rho_{ip}^{-1/3} \left(V \cos\theta - V_L\right) + C_{li} \rho_p^{-9/19} \left(\cos\theta\right)^{-18/19} \left(V_H - V \cos\theta\right) \tag{4}$$

where V_H – High velocity regime lower limit (km/s)
C_{hi} – Intermediate-high velocity fit coefficient (-)
C_{li} – Intermediate-low velocity fit coefficient (-)

Low velocity: when $V \leq V_L/\cos\theta$,

$$d_c = C_L \left(\cos\theta\right)^{-30/19} V^{-12/19} \rho_p^{-9/19} \tag{5}$$

where C_L – Low velocity fit coefficient (-)

For the enhanced zone 11 shield, the equation constants are given in Table 4.

Table 4: Constants of the FGB ballistic limit equation for the enhanced zone 11 shield.

V_L (km/s)	V_H (km/s)	C_L (-)	C_{li} (-)	C_{hi} (-)	C_H (-)
3	7	1.629	0.203	0.318	4.651

The diameter of steel wire used in the enhanced zone 11 shield was ~0.011", less than that of the DL-H configuration tested in this study (0.016"). As such, the ballistic limit equation constants must be adjusted in order to fit the test data. In Figure 17 the modified enhanced zone 11 ballistic limit equation is plotted along with the test results reported in Table 3 using the original equation constants defined in Table 4 and the adjusted equation constants, which are listed in Table 5. The low velocity and high velocity coefficients, C_L and C_H respectively, are calculated using the following relationships:

$$C_L = 3.11\left(t_w + \left(2AD_{mesh} + AD_{SP1} + AD_{SP2}\right)/2.8\right) \tag{6}$$

$$C_H = 3.52 + 3.0AD_{mesh} \tag{7}$$

Table 5: Modified constants of the FGB ballistic limit equation for the enhanced zone 11 shield.

V_L (km/s)	V_H (km/s)	C_L (-)	C_{li} (-)	C_{hi} (-)	C_H (-)
3	7	1.671	0.209	0.290	4.25

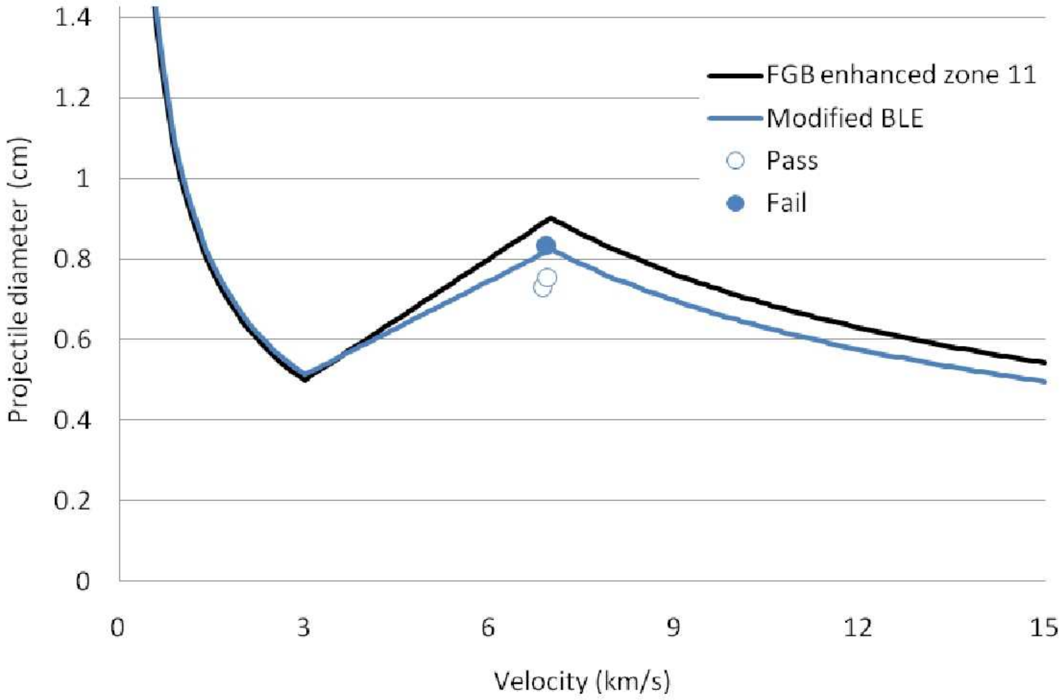

Figure 17: Ballistic limit curve (original and modified) of the DL-H configuration for normal impact.

The original ballistic limit equation constants are shown to over predict shielding performance at ~7 km/s (with normal incidence). Given that the original configuration used lower gauge wire in the mesh layers (0.011" diameter instead of 0.016"), this was expected. The original equation constants are therefore considered non-conservative for normal impact at ~7 km/s.

For the DL-F configuration the ballistic limit equation is modified to specify the areal densities of the specific shield components. For honeycomb sandwich panels, the mass of the honeycomb core is generally not used to determine effective shield thicknesses (i.e. the cores are treated as non-ballistic mass). For foam core sandwich panels, however, the foam is an active shielding component. The ballistic limit equation for the double-layer foam configuration is defined as:

High velocity: when $V \geq V_H/\cos\theta$,

$$d_c = C_H \left(V \cos\theta\right)^{-\beta} \rho_p^{-1/3} \tag{8}$$

where β – High velocity angle dependence constant (-) = 0.55

$C_H = 3.0 + 2.4 \times AD_{mesh}$

Intermediate velocity: when $V_L/\cos\theta > V > V_H/\cos\theta$,

$$d_c = d_c\left(V_L\right) + \frac{d_c\left(V_H\right) - d_c\left(V_L\right)}{V_H - V_L} \cdot \left(V - V_L\right) \tag{9}$$

Low velocity: when $V \leq V_L/\cos\theta$,

$$d_c = C_L\left(\cos\theta\right)^{-\alpha} V^{-12/19} \rho_p^{-9/19} \tag{10}$$

where α – Low velocity angle dependence coefficient (-) = 1.75

$C_L = 3\left(t_w + \left(2AD_{mesh} + AD_{SP1} + AD_{SP2}\right)/2.8\right)$

In Figure 18 through Figure 20 the ballistic limit curve calculated using Eq. (8)-(10) is shown along with test results (from Table 3). At normal incidence the curve shows a clear increase in performance in the intermediate (shatter) regime, indicating behavior similar to a multiple-wall shield. The curve is slightly conservative at ~7 km/s, predicting failure for impact of a 0.877 cm diameter projectile – conditions at which the target rear wall was heavily deformed yet not perforated or spalled. At 45°, the performance gain with increasing velocity in the shatter regime is significantly reduced. The curve is shown to fit the test data well, accurately predicting the failure limits at ~7 km/s (between 0.837 cm and 0.873 cm). At higher incidence (i.e. 60°) the equation correctly predicts failure limits at the onset of the transition regime. There is no test data for higher velocities.

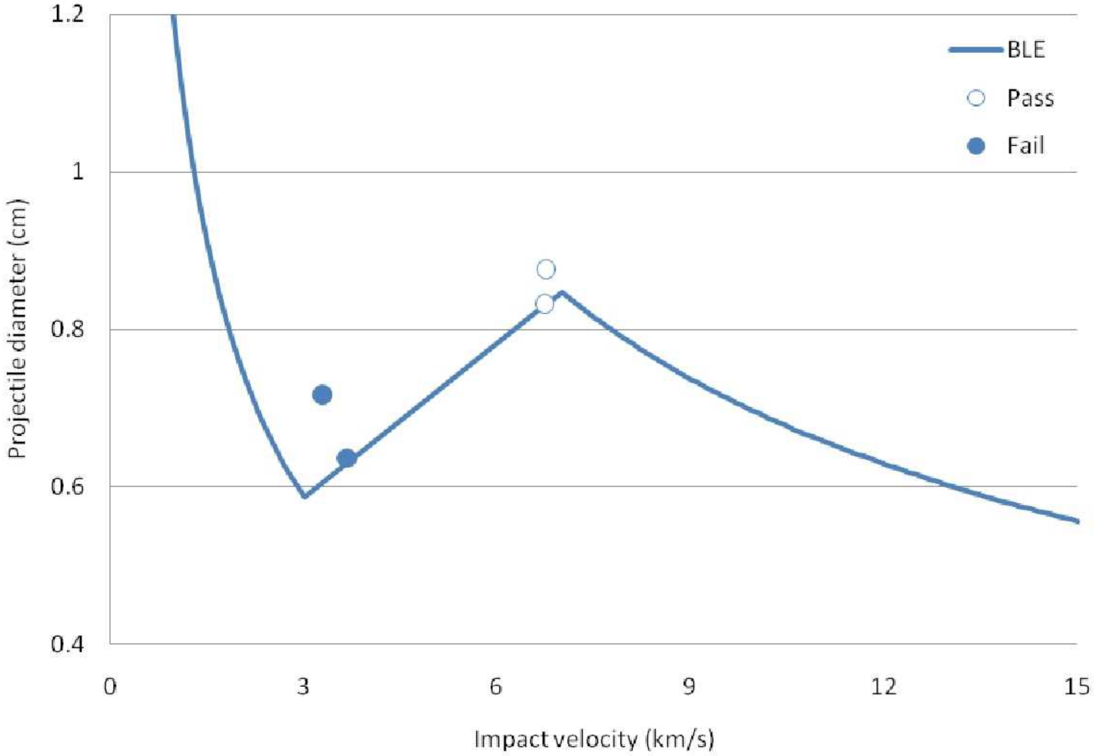

Figure 18: Ballistic limit curves of the double-layer foam shielding configuration at 0°.

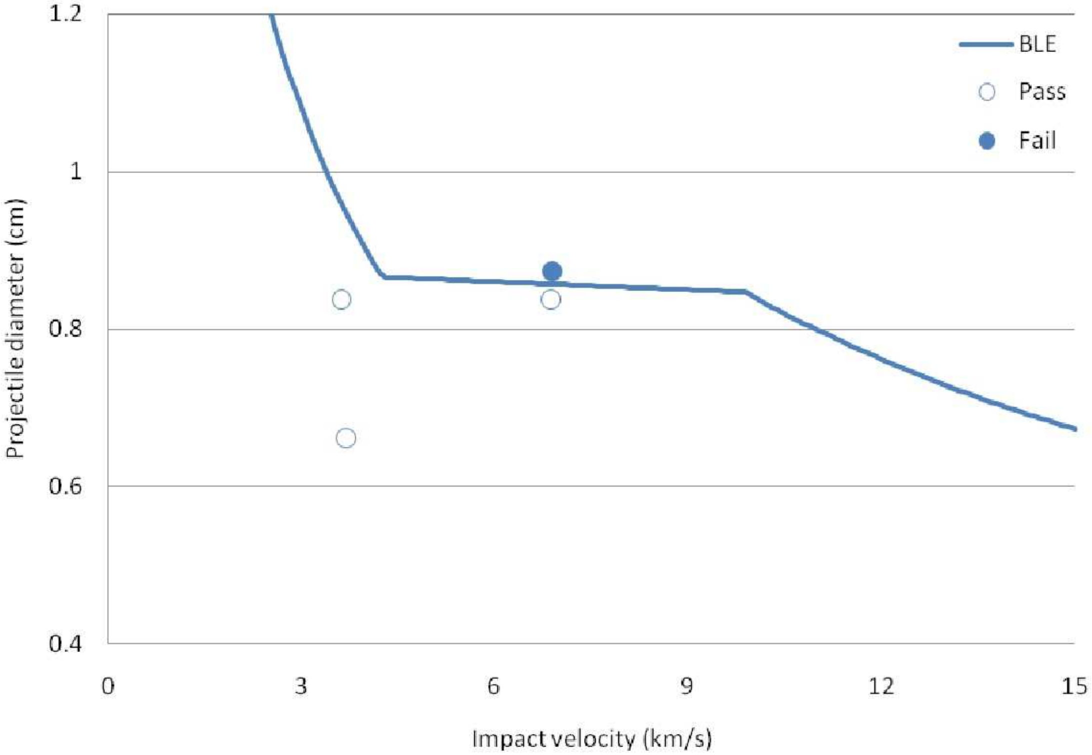

Figure 19: Ballistic limit curves of the double-layer foam shielding configuration at 45°.

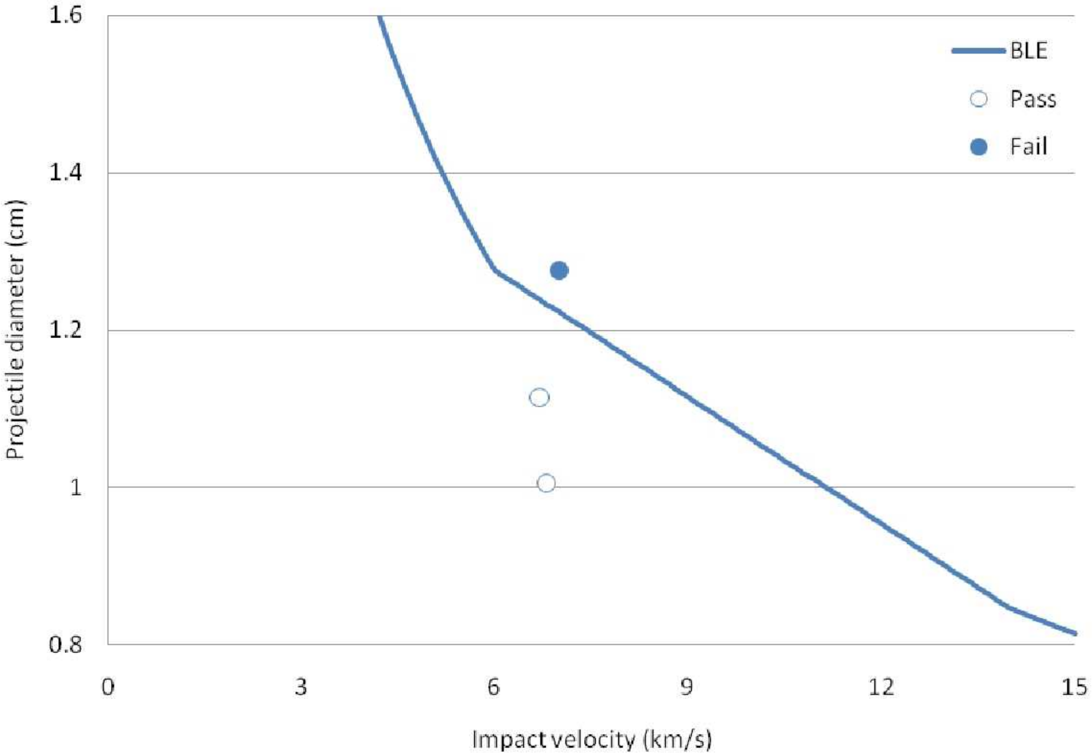

Figure 20: Ballistic limit curves of the double-layer foam shielding configuration at 60°.

Additional Test Data

Additional testing was performed prior to this study on double-layer foam and double-layer honeycomb configurations with lower gauge steel mesh layers. In these tests the wire diameter was 0.009" (instead of the 0.016" diameter used in this study), however the rest of the target components were nominally-identical. The areal density of the 30×30 SS304 mesh (∅ = 0.009") is equal to 0.078 g/cm^2. A summary of the impact test data is given in Table 6.

Table 6: Additional hypervelocity impact test results.

	Reference	Target	Angle (deg)	Projectile		Impact Velocity (km/s)	Result (P/SP/NP)
				Material	Diameter (mm)		
1	HITF03141	DL-H	0	Al2017-T4	0.794	6.82	NP
2	HITF03142	DL-H	0	Al2017-T4	0.913	6.86	P
3	HITF04165	DL-H	0	Al2017-T4	0.635	6.67	NP
4	HITF03143	DL-F	0	Al2017-T4	0.794	6.74	P
5	HITF03144	DL-F	0	Al2017-T4	0.794	6.71	P

A comparison between HITF03143 and HITF07460 shows that the mesh diameter can have a significant effect on shielding performance. The ballistic limit curve of the 0.016" diameter wire mesh and 0.009" diameter wire mesh DL-F and DL-H targets is shown in Figure 22. At 7 km/s the heavier mesh provides an 8.2% and 13.3% increase in perforation limit for the DL-F and DL-H targets respectively.

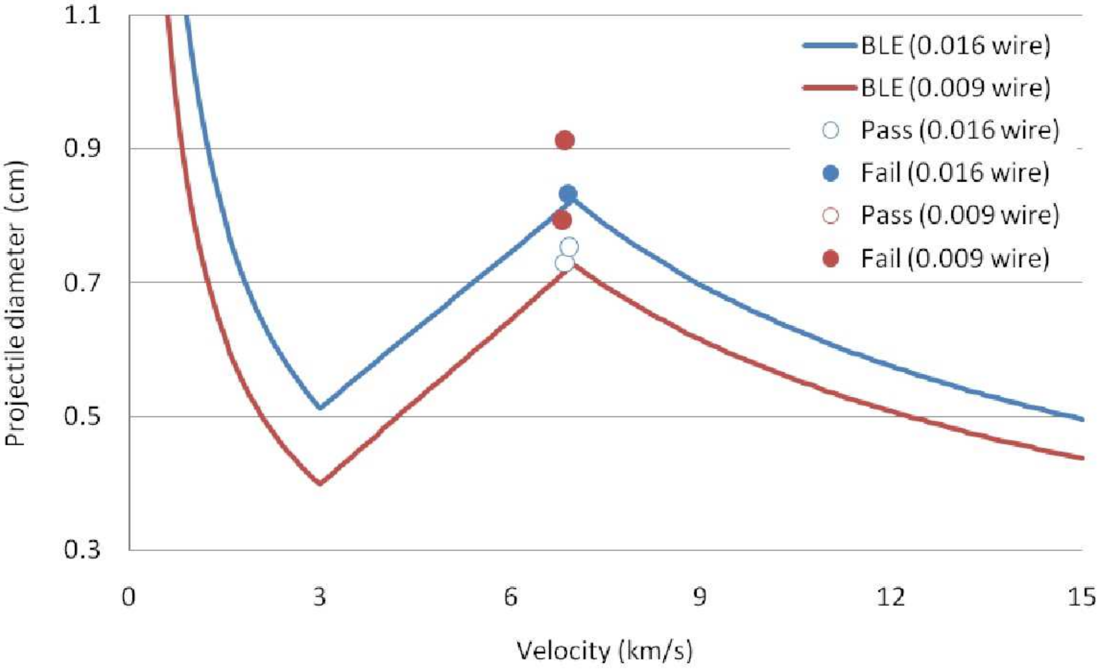

Figure 21: Ballistic limit curve of the DL-H shield with 0.009" and 0.016" diameter wire mesh layers.

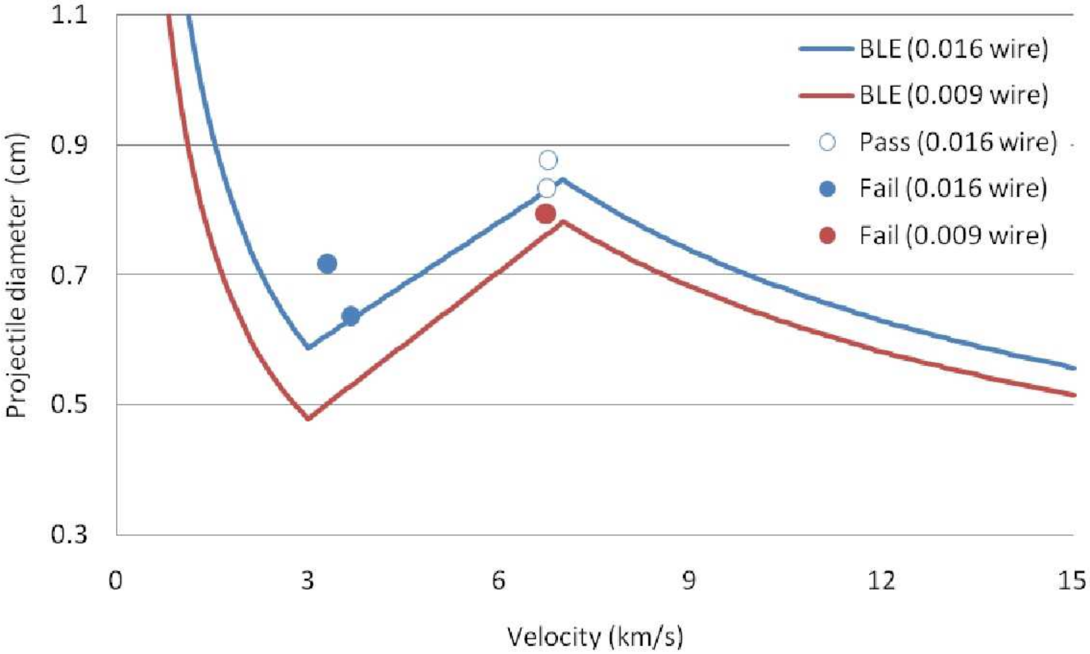

Figure 22: Ballistic limit curve of the DL-F shield with 0.009” and 0.016” diameter wire mesh layers.

Comparison of DL-H and DL-F Ballistic Limit Predictions

The modifications to the double-layer honeycomb sandwich panel configuration can be further assessed through comparison of the ballistic limit curves for the two configurations. In the event of a mission risk analysis, these equations would be used to assess the probability of penetration and catastrophic failure of the applicable vehicle, which would then be used to evaluate mission compliance with allowable risk figures. In Figure 23 through Figure 25 the modified enhanced zone 11 FGB ballistic limit equation is plotted against the equation derived for the DL-F configuration (in both cases 0.016” diameter wire meshes are considered). For normal impact, the modifications result in a small predicted improvement over the range of applicable impact velocities. At 3 km/s the shield modifications provide a 15% increase in critical projectile diameter, while at 7 km/s a 3% increase is predicted. The larger low velocity sizing constant C_L also leads to increasing performance gain with increasing impact velocity, although there is a lack of test data to support or disprove this extrapolation. At oblique impact the increase in low velocity performance enhancement increases as a result of the difference in defined angle dependence (-2/3 vs. -0.55 for the DL-H and DL-F shields respectively). At 45° the predicted performance enhancement of the DL-F shield is 22% over the baseline DL-H shield, which increases to 29% at 60°. For the DL-H configuration there was no test data generated in this study at low velocities. The low velocity fit coefficient (C_L) was defined to provide consistency with the original enhanced zone 11 coefficient.

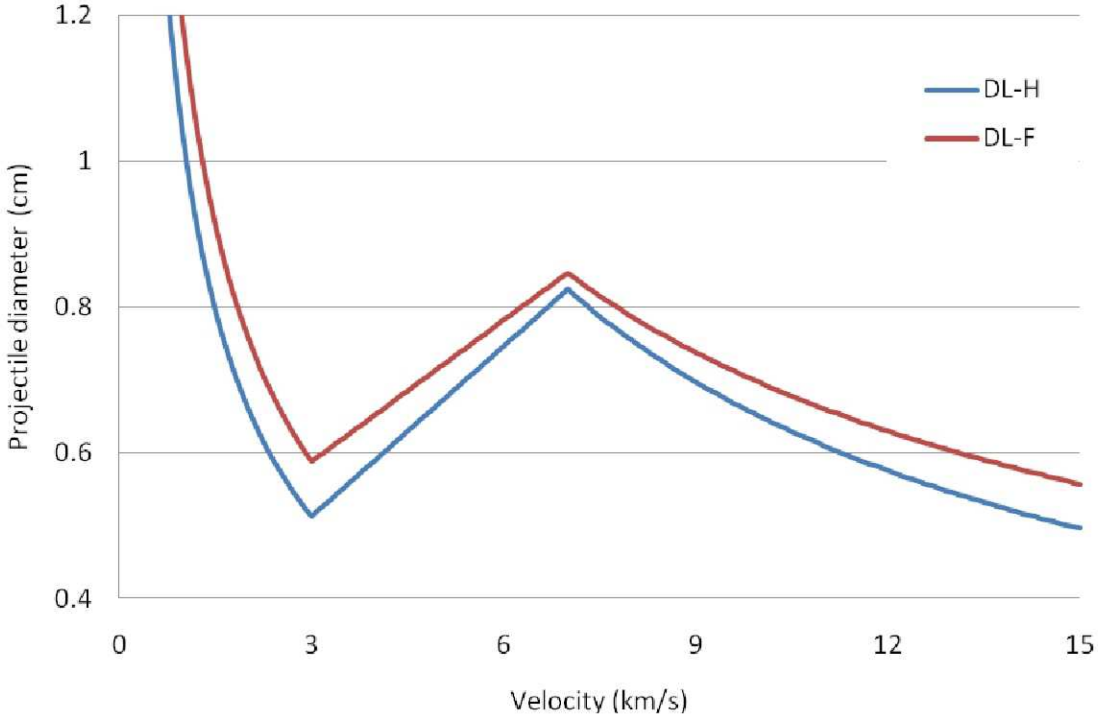

Figure 23: Comparison between the DL-H and DL-F ballistic limit curves at 0°.

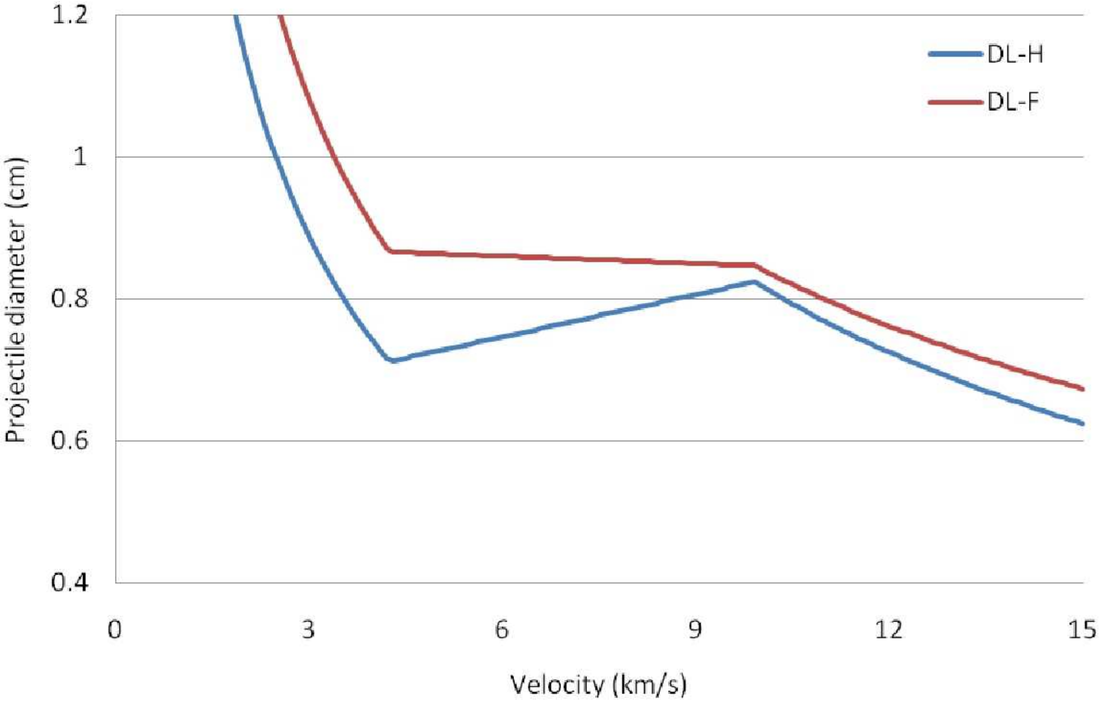

Figure 24: Comparison between the DL-H and DL-F ballistic limit curves at 45°.

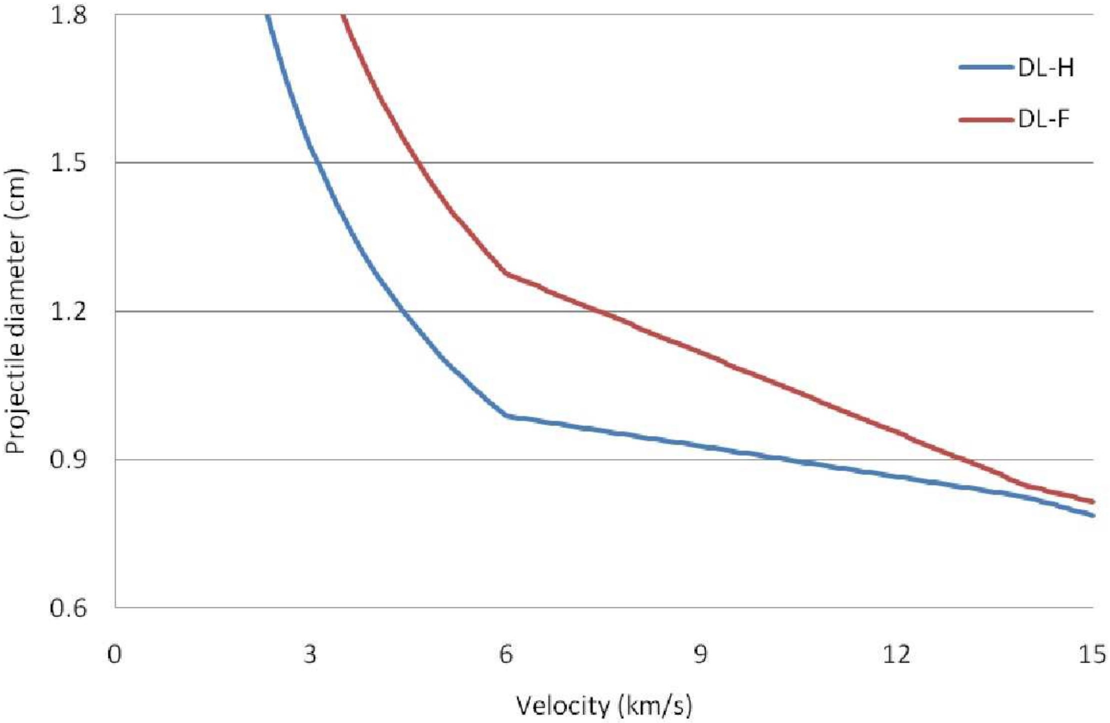

Figure 25: Comparison between the DL-H and DL-F ballistic limit curves at 60°.

Discussion

The ballistic limit equations defined for the DL-F and DL-H configurations are based on the JSC Whipple shield equation [13] which separates performance into the three velocity regimes: low, intermediate (or shatter), and hypervelocity. At low velocities, pressures generated during impact on the bumper plate are insufficient to cause projectile fragmentation, leading to impact of an intact (albeit deformed) particle upon the shield rear wall. Transition to the shatter regime occurs once pressures are large enough to induce projectile fragmentation via tensile release waves reflected from the bumper (or projectile) free surfaces (depending on impact geometry). Increasing impact velocity within the shatter regime leads to increased projectile fragmentation, resulting in a more finely dispersed debris cloud of smaller and more uniform particles. Incipient melting of projectile and bumper fragments also occurs in the shatter regime, the degree of which increases with increasing impact velocities. Until this point, failure of the Whipple shield rear wall results from the penetration of individual projectile or bumper fragments through cratering and spallation mechanisms. The transition from shatter to hypervelocity impact regime occurs once the rear wall failure mechanism switches from a cratering-type failure to that of an impulsive blast wave. Increasing impact velocity in the hypervelocity regime increases the kinetic energy of the impulsive load, resulting in a decrease in performance that scales (according to NASA practice) with kinetic energy.

Previous studies (e.g. [14]) have defined the onset of projectile melt to occur at ~5.6 km/s (for aluminum-on-aluminum impact), based on planar shock wave theory. For metallic foams, it is considered that secondary impacts of projectile and bumper fragments leads to an increase in shock heating (entropy), effectively decreasing material failure strength and leading to increased fragmentation, melting, and vaporization at lower impact velocities. Destefanis et al. [15]

reported on tests against a dual wall configuration with a bumper of open cell aluminum foam. In the tests a good deal of melting was observed at velocities as low as 2 km/s, with complete melting reported at velocities as low as 4 km/s. Similar enhanced fragmentation was reported in [16] for mm-sized projectiles at normal impact. However, this mechanism was not effective against projectiles in the cm-sized range, nor was it effective for oblique impacts. In this study, clear evidence of melted deposits was observed on the target rear wall for test #4 (HITF08595), performed at 3.29 km/s. For low velocity impacts at oblique impact (e.g. test #6 (HITF08596)) there is also clearly observable deposits of melted aluminum upon the shield rear wall. Although the onset and degree of projectile and bumper melt is clearly increased by the open-cell foam bumpers, in all impact tests performed there is evidence of solid fragment impacts upon the target rear walls. For oblique impacts, these solid fragment craters are generally in-line with the projectile velocity vector, indicating that they are most likely projectile remnants (see Figure 26).

Figure 26: Solid fragment craters on the DL-F rear wall at high impact velocities (0.877 cm diameter Al2017-T4 sphere at normal incidence with 6.76 km/s).

Destefanis et al. [16] defined the transition limits of the low and hypervelocity impact regimes at 2.7 and 6.5 km/s respectively, in recognition of the increased fragmentation and melting induced by the open cell foam bumper (compared to a traditional Whipple shield). Although (as discussed) increased fragmentation and melting was also observed for the double-layer foam configuration evaluated in this study, evidence of individual solid fragment cratering was found for impacts up to 6.76 km/s at normal incidence. In the absence of additional test data providing clear experimental justification, the transition velocities defined in [13] for aluminum Whipple shields and in [12] for the DL-H configuration are maintained in ballistic limit equation derived in this report.

The performance of aluminum open-cell foam bumpers was found to decrease for impact of cm-sized projectiles at normal incidence, and mm-sized projectiles at oblique incidence in [15]. The authors concluded that secondary impacts were no longer able to induce fragmentation and melting of the entire projectile at these impact conditions. In this study, however, there was no noticeable decrease in performance at obliquity, even for projectiles considerably larger than 1 cm in diameter (e.g. test #11 (HITF09064)). The double layer of mesh on top of the 1st sandwich panel of the DL-F configuration is expected to break up the projectile prior to impact on the sandwich panel facesheet. Therefore, smaller projectile fragments are propagated to impact within the sandwich panel foam core and the size-limitations of secondary fragmentation and melting discussed by Destefanis et al. are not valid.

Conclusions

The purpose of this study was to evaluate the effect on shielding performance achieved by replacing metallic honeycomb cores for metallic open-cell foam cores in a double sandwich panel MMOD shielding configuration representative of those used onboard the ISS. Towards this goal 19 hypervelocity impact tests were performed on double-layer honeycomb and foam configurations, from which ballistic limit equations were defined based on the JSC Whipple shield equation [13] and FGB generic ballistic limit equation [12]. The double-layer honeycomb configuration was similar to the enhanced zone 11 shield on the FGB, reported on in [12]. However, the ballistic limit equation constants implemented in BUMPER were found to be non-conservative at velocities around 6-7 km/s. As such, modified parameters were defined for the double-layer honeycomb (aka enhanced zone 11) configuration. For the double-layer foam configuration new constants for the FGB ballistic limit equation were empirically derived from the test data. The low velocity fit coefficients are derived from the areal densities of the individual shield components, enabling their application on modifications to the original shield. Test data on the double-layer foam configuration incorporating mesh layers constructed with smaller diameter wires than used in the baseline configuration were used to evaluate the accuracy of the low velocity constant calculation, and good agreement with the test data was shown.

At normal incidence the foam-modified shield was found to provide a 15% improvement in critical projectile diameter at low velocity (i.e. 3 km/s) and a 3% increase at high velocity (7 km/s). With increasing impact obliquity the foam shield performance enhancement increases at the low-shatter regime transition velocity, up to a 29% improvement in critical diameter at 60°. It should be noted that the double-layer honeycomb equation constants are defined for consistency with the enhanced zone 11 shield described in [12], for which there is no low velocity test data.

The presence of honeycomb cells is considered to be detrimental to the shielding performance of a dual-wall configuration due to the cell walls acting to restrict the expansion of projectile and bumper (or front facesheet) fragments – referred to as channeling. However, the thickness of the honeycomb sandwich panels in the double-layer configuration are less than twice the diameter of even the smallest projectile used in the testing. Thus, dispersion of the projectile and bumper fragments is expected to be uninterrupted prior to impact upon the sandwich panel rear facesheet. As such, the performance enhancement gained by replacing the honeycomb core with open-cell foams is not expected to result as a simple absence of through-thickness channeling cells. Rather, secondary impacts of projectile and bumper fragments upon individual foam cell ligaments induced repeated shocks, increasing fragment entropy and subsequently reducing failure strengths. Evidence of increased projectile fragmentation and melting was shown for the double-layer foam configuration (compared to the double-layer honeycomb configuration). Previous investigations on metallic open-cell foam bumpers have noted a decrease in performance for oblique impact, and normal impact of large cm-sized projectile due to an inability of the repeated shocking procedure to fragment the entire projectile at these conditions. However, the presence of the double mesh outer layers breaks up the projectile prior to impact upon the 1st sandwich panel front facesheet, ensuring the propagation of smaller, more manageable impactors within the foam core.

References

[1] D.W. Jex, A.M. Miller, C.A. MacKay, “The Characteristics of Penetration for a Double-Sheet Structure with Honeycomb”, NASA Marshall Space Flight Center, Huntsville, NASA TM X-53974, 1970.

[2] J-M. Sibeaud, C. Thamie, C. Puillet, “Hypervelocity Impact on Honeycomb Target Structures: Experiments and Modeling”, International Journal of Impact Engineering; 35: 1799-1807, 2008.

[3] E.A. Taylor, M.K. Herbert, B.A. Vaughan, J.A. McDonnell, “Hypervelocity Impact on Carbon Fibre Reinforced Plastic / Aluminum Honeycomb: Comparison with Whipple Bumper Shields”, International Journal of Impact Engineering; 23(1): 883-893, 1999.

[4] S. Ryan, F.K. Schaefer, R. Destefanis, M. Lambert, “A Ballistic Limit Equation for Hypervelocity Impacts on CFRP/Al HC Satellite Structures“, Advances in Space Research; 41: 1152-1166, 2008.

[5] R. Sennett, B. Lathrop, “Effects of Hypervelocity Impact on Honeycomb Structure”, Journal of Spacecraft; 5(12): 1496-1497, 1968.

[6] B. Cour-Palais, “Meteoroid Protection by Multiwall Structures”, AIAA Hypervelocity Impact Conference, Cincinnati, April 30-May 2, AIAA Paper No. 69-372, 1969.

[7] R. Destefanis, “Enhanced Space Debris Shields for Manned Spacecraft – Evaluation Report: Phase A and Phase B Tests”, Alenia-Spazio, Turin, ESD-TN-AI-005, 2004.

[8] J. Yasensky, E.L. Christiansen, T. Prior, “Hypervelocity Impact Evaluation of Metal Foam Core Sandwich Structures”, GeoControl Systems, Houston, NASA TP-2008-214776, 2008.

[9] E. Andrews, W. Sanders, L. Gibson, “Compressive and Tensile Behaviour of Aluminum Foams”, Materials Science and Engineering; A270: 113-124, 1999.

[10] B.G. Cour-Palais, J.L. Crews, “A Multi-Shock Concept for Spacecraft Shielding”, International Journal of Impact Engineering; 10: 135-146, 1990.

[11] H.F. Swift, “Hypervelocity Impact Mechanics”, in: Impact Dynamics (Zukas, ed.), John Wiley & Sons, New York, 1982.

[12] G.A. Sanchez, E.L. Christiansen, “FGB Energy Block Meteoroid and Orbital (M/OD) Debris Shield Test Report”, NASA Johnson Space Center, Houston, JSC Document 27460, 1996.

[13] E.L. Christiansen, “Design and Performance Equations for Advanced Meteoroid and Debris Shields”, International Journal of Impact Engineering; 14(1-4): 145-156, 1993.

[14] A.K. Hopkins, T.W. Lee, H.F. Swift, “Material Phase Transformation Effects upon Performance of Spaced Bumper Systems”, Journal of Spacecraft and Rockets; 9(5): 342-345, 1972.

[15] R. Destefanis, F. Schaefer, M. Lmabert, M. Faraud, E. Schneider, “Enhanced Space Debris Shields for Manned Spacecraft”, International Journal of Impact Engineering; 29: 215-226, 2003.

[16] R. Destefanis, F. Schaefer, M. Lambert, M. Faraud, “Selecting Enhanced Space Debris Shields for Manned Spacecraft”, International Journal of Impact Engineering; 33: 219-230, 2006.